ALUMINUM CHLORINE BATTERY

BY JOSÉ GINER AND GERHARD L. HOLLECK

June 1970

Prepared under Contract No. NAS 12-688 by

TYCO LABORATORIES, INC.
WALTHAM, MASSACHUSETTS 02154

ELECTRONICS RESEARCH CENTER
NATIONAL AERONAUTICS AND SPACE ADMINISTRATION

NASA

ALUMINUM CHLORINE BATTERY

By José Giner and Gerhard L. Holleck

Final Technical Report
Covering Period
27 May 1968 — 26 March 1970

Prepared under Contract No. NAS 12-688 by

TYCO LABORATORIES, INC.
Waltham, Massachusetts 02154

Electronics Research Center
NATIONAL AERONAUTICS AND SPACE ADMINISTRATION

Technical Monitor:
Dr. Sol Gilman,
Energy Conversion Materials Branch
NASA-Electronics Research Center
575 Technology Square
Cambridge, Massachusetts 02139

Requests for copies of this report should be referred to:

NASA Scientific and Technical Information Facility
P. O. Box 33
College Park, Maryland 20740

Table of Contents

Table of Contents (Cont.)

List of Illustrations

List of Illustrations (Cont.)

List of Illustrations (Cont.)

List of Illustrations (Cont.)

ALUMINUM CHLORINE BATTERY

By José Giner and Gerhard L. Holleck

Tyco Laboratories, Inc.
Waltham, Massachusetts 02154

SUMMARY

A molten salt system based on Al- and Cl_2-carbon electrodes, with an $AlCl_3$-alkali chloride eutectic as electrolyte, offers promise as a rechargeable, high energy density battery which can operate at a relatively low temperature and may withstand sterilization. To obtain pure $AlCl_3$-KCl-NaCl melts, different commercial $AlCl_3$ materials have been investigated. $FeCl_3$ was found to be the major impurity in all of them. A procedure involving treatment of a melt of high $AlCl_3$ concentration with magnesium powder or with in-situ generated, finely divided Al prior to evaporation yielded pure $AlCl_3$. $AlCl_3$-KCl-NaCl melts using this material stayed clear (nearly colorless), and showed practically no background current.

Measurements of electrolyte conductivity were made in the ternary melt. The temperature dependence of the specific conductivity from 125 to 185 °C in the melt $AlCl_3$-KCl-NaCl (57.5-12.5-30 mol %) can be represented by

$$\kappa_{sp} = 11.4 \pm 0.9 \exp\left(-\frac{3360 \pm 68}{RT}\right) \text{ohm}^{-1}\text{cm}^{-1}$$

Investigations of vitreous carbon electrodes have shown that carbon is intrinsically active for chlorine reduction in $AlCl_3$-alkali chloride melts. Using a rotating vitreous carbon disk electrode, the kinetic parameters were determined. It was found that the chlorine reduction occurs according to the paths:

$$Cl_2 + e^- \rightleftharpoons Cl^- + Cl \qquad (1)$$

and

$$Cl + e^- \rightleftharpoons Cl^- \qquad (2)$$

where Eq. (1) is the rate determining step. The apparent exchange currents were found to be 1×10^{-4} to 2×10^{-4} A/cm^2.

A study of the compatibility of carbon electrodes for chlorine in $AlCl_3$ eutectics has uncovered carbon samples which appear suited for the construction of porous chlorine cathodes.

Passivation phenomena have been observed upon cathodic and anodic polarization of the Al electrode in $AlCl_3$-KCl-NaCl melts. It was established that they are not due to an electrochemical (potential dependent) process, but rather are caused by formation of a solid salt layer at the electrode surface resulting from concentration changes upon anodic or cathodic current flow. The value of the steady-state current is determined by diffusion processes in the

melt and by the concentration change necessary to pass the liquidus curve of the phase diagram. The electrode behavior upon cathodic polarization is further complicated by dendrite growth which causes the electrode to expand into the melt. This was also confirmed by in situ observation of the Al electrode during polarization. The Al electrode itself was found to be quite reversible, as reflected in its apparent exchange current of 268 mA/cm^2 at 130 °C.

The feasibility of an aluminum/chlorine battery in the primary mode was also experimentally demonstrated.

INTRODUCTION

A great deal of effort, over the past 7 years, has been directed toward the development of batteries with energy densities of the order of 200 Whr/lb. The negatives in these high energy density systems are characteristically selected from the most electronegative of the metals. The use of electronegative metals such as Li or Na necessitates the use of electrolytes which are aprotic. Organic and molten salt media have both been used; however, since aprotic organic electrolytes can be used at ambient temperatures, these have received by far the greater amount of attention.

Major disadvantages of cells based on aprotic organic electrolytes are instability of positive plates (resulting in short shelf life) and low conductivity. The chief disadvantage of the molten electrolyte batteries presently investigated is the necessity for high temperature operation, which introduces many problems related to materials of construction, safety, etc. Furthermore, the insulation needed to keep these high temperature batteries in operating condition leads to a degradation of the energy density of the battery.

It seems possible to overcome the problems associated with the high working temperatures of the present molten salt systems, while still retaining the advantages of high energy density and relatively efficient electrode processes, by using a cell composed of an Al negative and a Cl_2 positive in a low temperature electrolyte of molten $AlCl_3$-KCl-NaCl. The operating temperature of this system would be in the range of 120 to 150 °C, with a theoretical energy density of 650 Whr/lb. Furthermore, it should be possible to obtain a cell operable at even lower temperatures by using, as electrolyte, a melt of $AlCl_3$ with one or more of the other alkali chlorides (LiCl, RbCl, CsCl), which are all lower melting than NaCl or KCl.

The theoretical energy density of 650 Whr/lb for the Al-Cl_2 system compares favorably with that of 754 Whr/lb for the Li-CuF_2 (propylene carbonate) system and 990 Whr/lb for the Li-Cl_2 (molten salt) system. Another advantage of the Al-Cl_2 system would be that solid Al is easier to handle and much less hazardous than molten Li or Na. The hazards of the Cl_2 electrode (common to both the Li-Cl_2 and the proposed new system) will be reduced to some extent by the lower working temperatures; the same methods suggested for this electrode in the high temperature cell (adsorption and occlusion on porous carbon or graphite) can be used here.

To devise a practical, workable cell, knowledge is required of the reactions that take place at the anode and cathode of the particular system, as well as knowledge of the electrolyte properties and of the interaction of the complete system.

In addition to demonstrating the feasibility of this kind of battery, it was our aim to optimize it and to define its limitations by determining the kinetic parameters of the electrodes and the pertinent physicochemical data of the electrolyte.

Properties of the Melts

$AlCl_3$ melts at a low temperature (190 °C), but has a very low conductivity [at 700 °C, $\kappa = 6.56 \times 10^{-6}$ $ohm^{-1}cm^{-1}$, and in the region of the melting point it is even lower (Ref. 1)]. However, it is possible to obtain a lower melting system with considerably increased conductivity by addition of NaCl and/or KCl.

The available data on $AlCl_3$-alkali halide eutectics are listed in Table I. It is obvious that much work has been done on the $AlCl_3$-NaCl, $AlCl_3$-KCl, and $AlCl_3$-KCl-NaCl mixtures. The other alkali halides, however, have received scant attention.

TABLE I

$AlCl_3$-ALKALI HALIDE EUTECTIC MELTS

System	Composition, mol %	Eutectic Melting Point, °C	Reference No.
$AlCl_3$-LiCl	60	114	10, 16
$AlCl_3$-NaCl	62	112	2, 4, 5, 6, 7, 8, 9, 10 12, 14, 15, 16
	60	115	
	59	123	
	50	150	
	66	93	
$AlCl_3$-NaCl	61	108	2, 4, 16
$AlCl_3$-KCl	67	128	1, 2, 4, 6, 8, 9, 10 13, 17
$AlCl_3$-KCl	71-65.5	114-149	16
$AlCl_3$-KCl-NaCl	60-14-26	93	2, 8, 3, 9, 16
	63.5-16.5-20	88-9	
	62.13-12.7-25.17	94	
	66-14-20	70	
$AlCl_3$-RbCl			
$AlCl_3$-CsCl	74.6	148	11

Thermal analyses of the $AlCl_3$-KCl-NaCl system have been carried out (Refs. 2 and 3). The complete phase diagram, taken from Ref. 2, is shown in Fig. 1, and several cross sections from it are shown in Fig. 2. As can be seen from Table I, the lowest melting eutectic in the $AlCl_3$-KCl-NaCl system is formed between the intermediate compounds $KAlCl_4$, $NaAlCl_4$, and $AlCl_3$. Its melting point was reported to be 70 °C at an approximate composition of 66 mol % $AlCl_3$, 14 mol % KCl, and 20 mol % NaCl. Reference to Table I reveals that little is known about the $AlCl_3$-rich region, i.e., the low temperature region of the phase diagram. In this

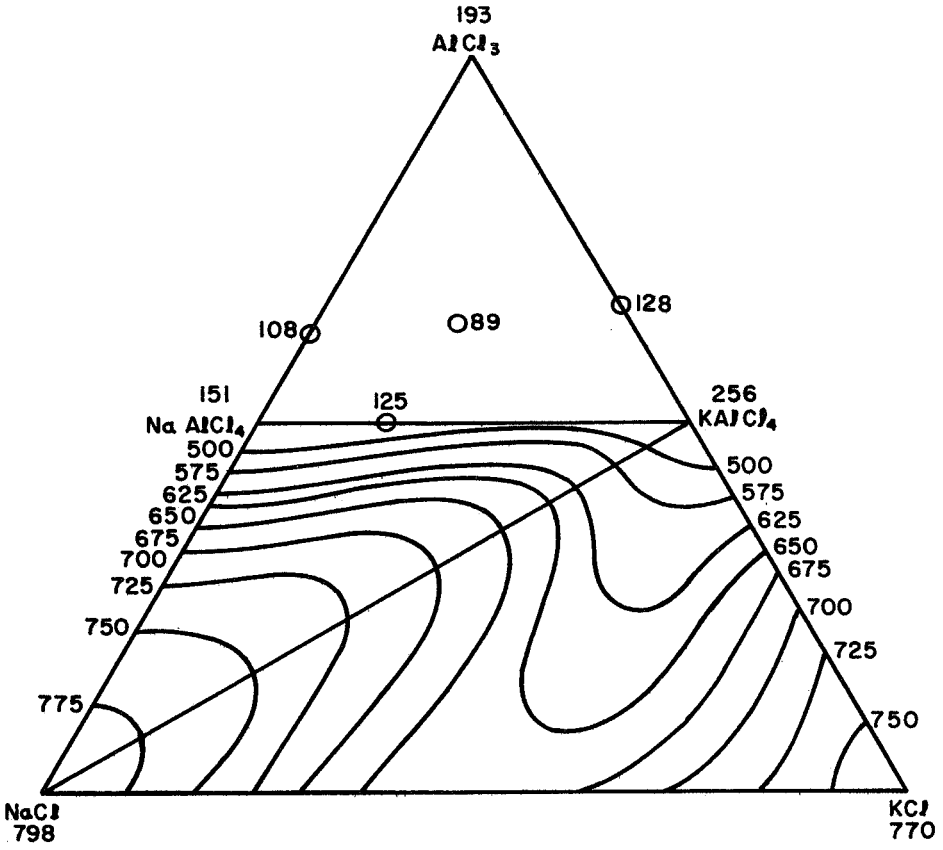

Fig. 1. Phase diagrams for the system $AlCl_3$-KCl-NaCl [O = eutectic, temperature = °C; data from Fischer and Simon (Ref. 2)]

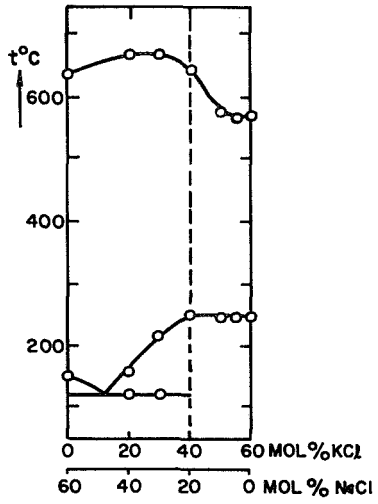

(a) Section through ternary system at 49 mol % $AlCl_3$

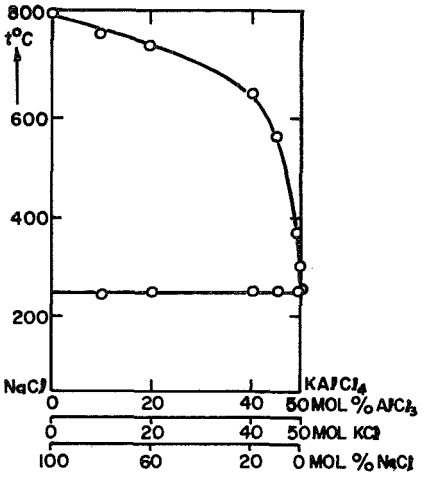

(b) Pseudobinary section NaCl-$KAlCl_4$

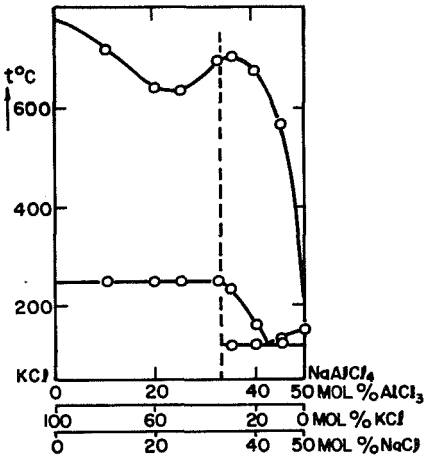

(c) Section KCl-$NaAlCl_4$

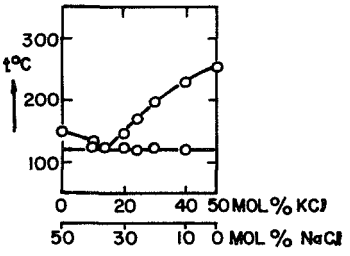

(d) Section through ternary system at 50 mol % $AlCl_3$ (pseudobinary system $NaAlCl_4$-$KAlCl_4$)

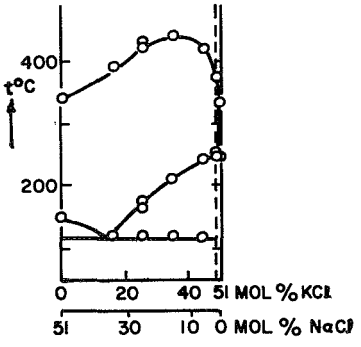

(e) Section through ternary system at 40 mol % $AlCl_3$

Fig. 2. Cross sections from the phase diagram for the system $AlCl_3$-KCl-NaCl

region, we can anticipate a rather high vapor pressure of $AlCl_3$, since not all of the $AlCl_3$ will be present as the complex $AlCl_4^-$. It has, however, been proposed (Ref. 3) that in an $AlCl_3$-rich melt the following solvation process takes place:

$$AlCl_3 + AlCl_4^- \rightleftharpoons Al_2Cl_7^-$$

Conductivity and density measurements have been carried out by Midorikawa (Ref. 18) on the ternary melt. In the temperature range 130 to 205 °C and composition range 21.3 to 40.4 mol % NaCl and 5.8 to 23.9 mol % KCl, the conductivity lies between 0.365 and 0.118 $ohm^{-1}cm^{-1}$. The relation between κ and temperature is approximately linear in this range. Midorikawa states that the large contribution to the conductivity of the ternary mixtures is made by NaCl; the contribution from KCl is only 50% of that made by NaCl. Analogy with the binary melts suggests that maximum conductivity should occur at the composition $NaAlCl_4$. $KAlCl_4$ (i.e., 50 mol % $AlCl_3$, 25 mol % NaCl, and 25 mol % KCl).

Melts containing $AlCl_3$, NaCl, and KCl are stable, and they have been used as reaction media for organic reactions [e.g., addition of KCl to C_2H_4 (Ref. 19)]. It appears that these melts can be used in Pyrex (or Vycor) glass at temperatures up to 700 °C (Refs. 2, 19, and 20). At temperatures up to 800 °C, Grothe (Ref. 11) used a quartz reaction vessel. On the other hand, Fischer and Simon (Ref. 2) reported that, when an $AlCl_3$-NaCl melt with the $NaAlCl_4$ composition was electrolyzed in quartz crucibles, corrosion of the crucibles occurred. They concluded that this was due to Al, or low valency Al compounds, dissolved in the melt. The species of Si dissolved in the melt was not identified.

Preparation and Purification of $AlCl_3$-KCl-NaCl Melts

All experimental work was carried out in the argon atmosphere of a "Lab Con Co.," purge-type glove box connected to a Tyco-built pressure control system. Analyzed argon with a water content of less than 1.5 ppm was used. "Baker Analyzed" NaCl and KCl were employed, but $AlCl_3$ from a number of different suppliers was tried.

Our first experiments were conducted with the ternary eutectic of composition 66 mol % $AlCl_3$, 14 mol % KCl, and 20 mol % NaCl. "Baker Analyzed" anhydrous $AlCl_3$ was used (this was certified as being 99% pure). The salts were weighed out in correct portions, well mixed, and fused on a hotplate. A greyish-brown melt was readily formed.

Other investigators (Ref. 21) have also observed this coloration, and attribute it to carbonaceous material and the presence of $FeCl_3$ impurity in the $AlCl_3$. Filtration of the molten eutectic through a fine (25-μ) glass frit did not appear to change the color at all, but did remove some particulate matter.

Cyclic scans at a Pt wire microelectrode were run to observe the background current and to obtain an indication of the nature of the impurities. The cyclic scans were recorded in the usual manner: a triangular waveform from a function generator (Exact Electronics, Inc., type 255) was fed into the input of a Wenking potentiostat (type 61RS). The potentiostatic current-voltage curves were recorded on an x-y recorder (Houston Omnigraphic model HR-98T).

Galvanostatic polarization curves were obtained by supplying a constant current from a power supply, and recording the overpotential on either an oscilloscope or on the x-y recorder.

It has been established (Refs. 22 and 23) that an Al electrode is a stable reference in this ternary eutectic, and all potentials are referred to this electrode. The actual reference electrode consisted of a coil of pure Al wire in a fritted compartment (to prevent concentration changes from taking place in the vicinity of the electrode). A similar coil of Al wire served as counterelectrode. The Pt needle electrode was made in the usual way, by sealing Pt into glass.

A typical current-voltage scan is shown in Fig. 3. The anodic decomposition limit was approximately +2 V versus Al, and corresponds to Cl_2 evolution. The reduction wave at +1 V versus Al was suspected to be due to the reduction of ferric ions. The addition of Al powder resulted in a marked reduction of the background current, probably by the reaction

$$Al + Fe^{3+} \rightarrow Fe + Al^{3+}$$

For subsequent measurements, $AlCl_3$ was obtained from Fluka Chemicals (Switzerland). It was stated to be anhydrous and iron-free. A ternary mixture made up with this material melted readily on a hotplate and formed a clear melt, except for a darkish yellow coloration. A cyclic scan obtained in this melt is shown in Fig. 4. It appears that $FeCl_3$ is still present as an impurity. The deliberate addition of a small amount of $FeCl_3$ resulted in the current-voltage curve shown in Fig. 5.

The curves of both Figs. 4 and 5 were obtained on Pt electrodes starting at a potential of 1.1 V versus Al. From this starting point, the potential was linearly decreased to zero, then increased linearly to 2 V, and then decreased again, without a waiting time, to 1.1 V. Based on this qualitative agreement, we suggest the following tentative assignment of the various characteristics of the curve of Fig. 4 to the different states of oxidation of iron.

1. A more or less pronounced cathodic current peak was observed at about 1 V, probably due to reduction of Fe^{3+} incorporated in some layer close to the electrode.

2. Cathodic limiting current at more negative potentials appeared to correspond to the steady-state reduction of Fe^{3+} to Fe^{2+}.

3. A cathodic peak at about 300 mV could possibly be due to the reduction of Fe^{2+} (or Fe^{3+}) to Fe^{+}, followed by further reduction to Fe at potentials below approximately 200 mV. (If the electrode was potentiostatically held at 100 mV prior to an anodic sweep, a proportionality between the time at 100 mV and the anodic peak height at 500 mV was observed. This was not the case if the electrode was held at approximately 200 mV.)

4. An anodic peak at about 500 mV apparently corresponded to oxidation of Fe to Fe^{2+}. The current drop after the peak can be attributed to depletion of Fe or to some passivation.

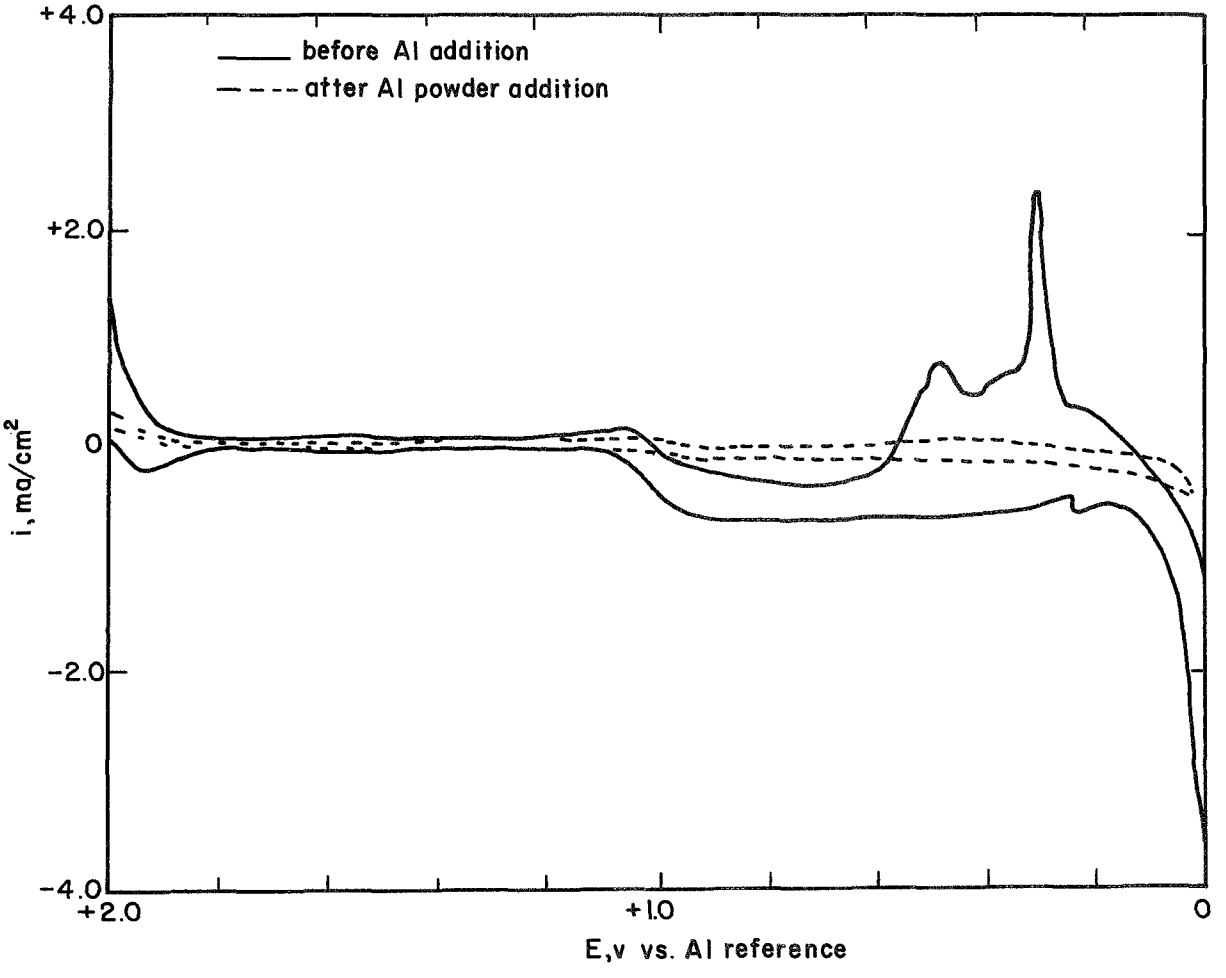

Fig. 3. Background i-V scan at Pt in eutectic melt (Baker Analyzed $AlCl_3$, 99% anhydrous; scan rate = 40 mV/sec)

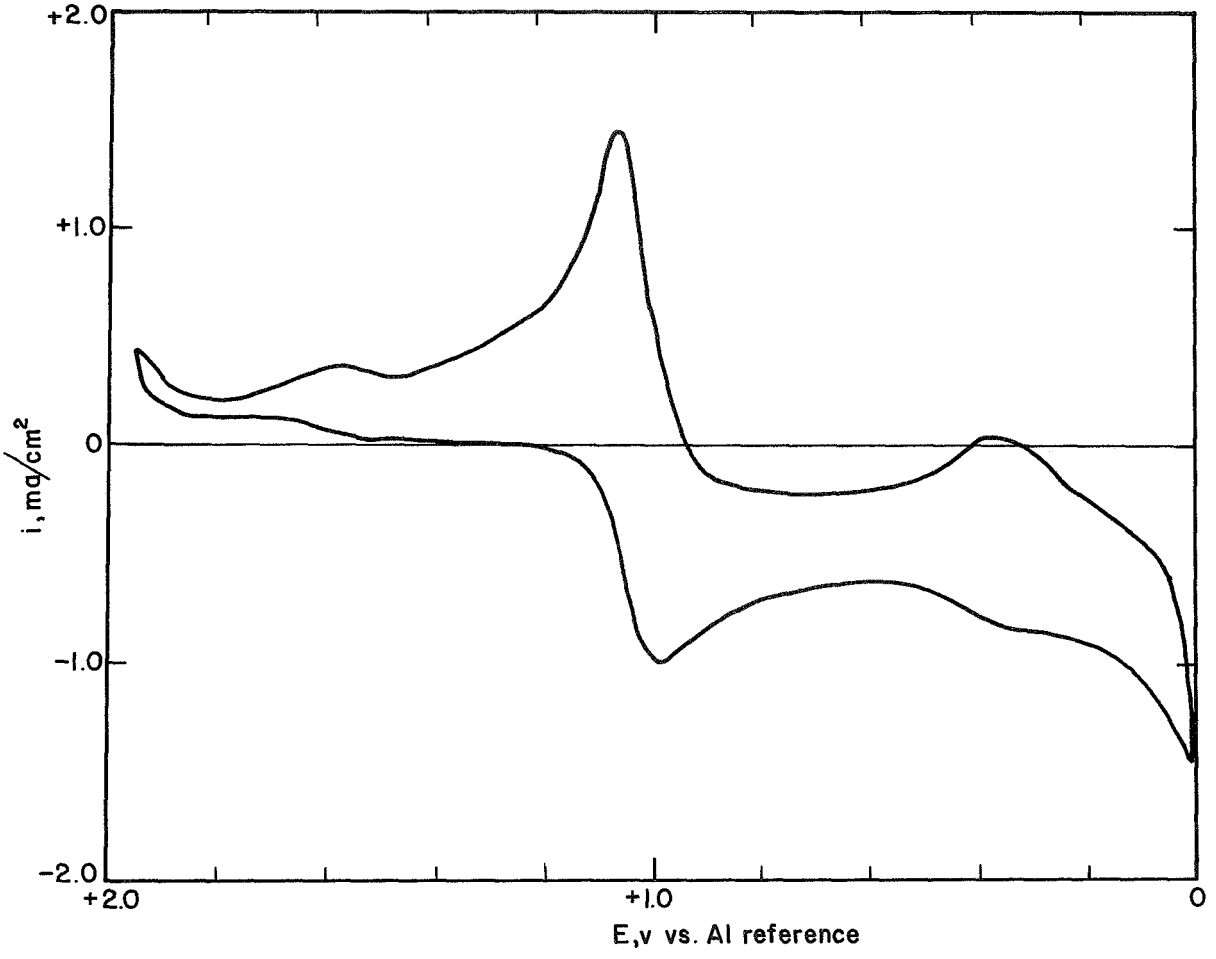

Fig. 4. Background i-V scan at Pt in eutectic melt (Fluka $AlCl_3$, anyhydrous and "iron-free"; scan rate = 160 mV/sec)

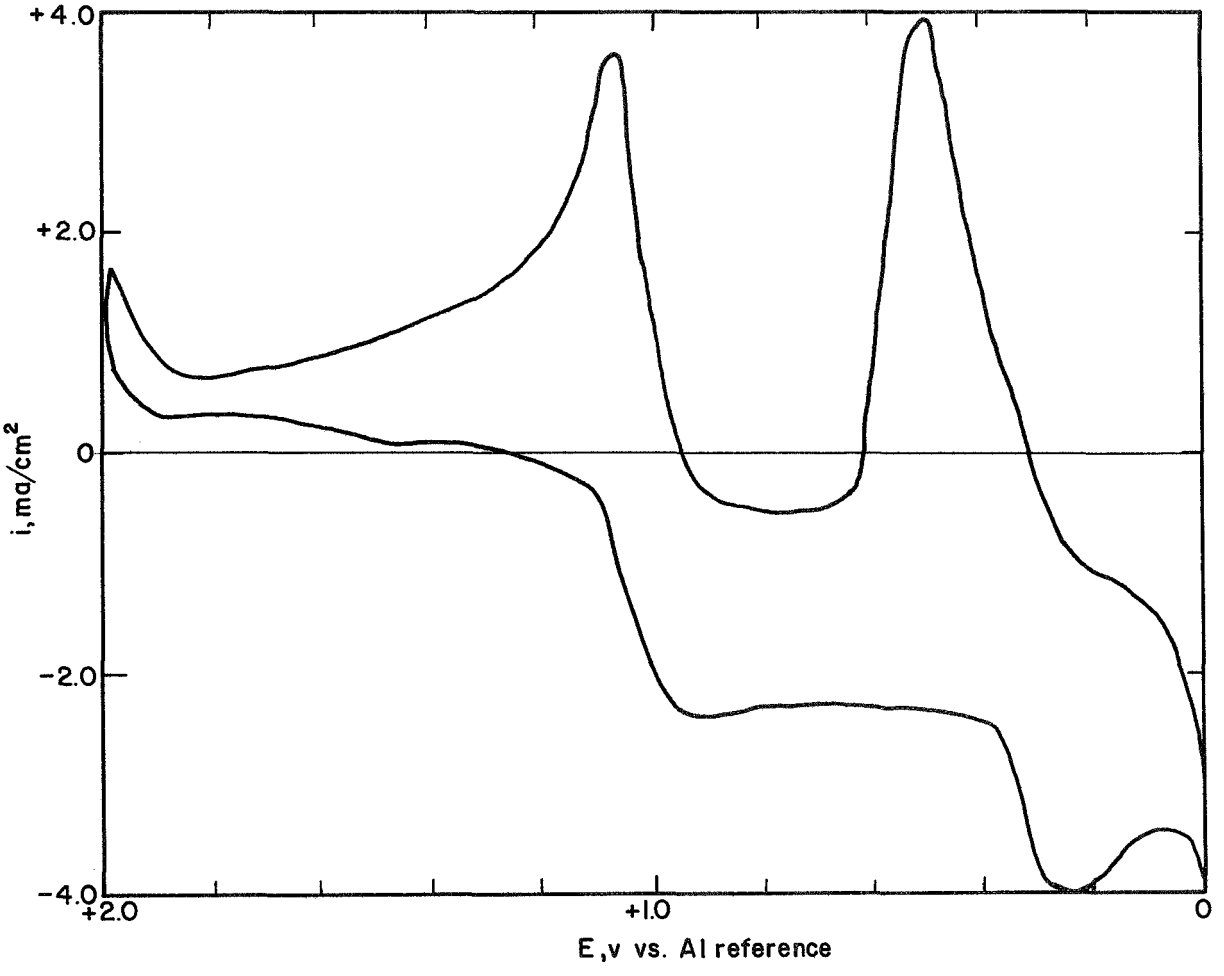

Fig. 5. Effect of small addition of $FeCl_3$ to eutectic melt (Fluka $AlCl_3$; scan rate = 160 mV/sec)

5. After this passivation, a relative cathodic current is observed that can be attributed to reduction of Fe^{3+}.

6. Finally, the anodic peak at 1.1 V can be interpreted as being due to oxidation of Fe^{2+} to Fe^{3+}. Further, if a passive film existed, it, and the possibly underlying Fe, are oxidized here. Any dissolved Fe^{2+} is oxidized to Fe^{3+} at potentials higher than 1.2 V.

From the comparison of Figs. 4 and 5, it seems reasonable to identify the major impurity present in $AlCl_3$ as Fe.

The change of coloration may be due to several factors: (1) the formation of colloidal hydroxides of heavy metals as the melt absorbs water, (2) a higher degree of oxidation of these impurities, or (3) decomposition of organic material. Thus, in order to obtain satisfactorily clean eutectics, we have studied first the behavior of a large number of electrolytes prepared with several $AlCl_3$ samples obtained from different manufacturers: Mallinckrodt lot RTY and TJB, Fisher lot 780679, MCB lot 25, Baker and Adamson lot B128, J. T. Baker lots 33025 and 33824, BDH (Gallard-Schlesinger, N.Y.) lot 0564110, Fluka (Buchs, Switzerland) lot 461085, Koch-Light Labs (Colnbrook, Buckinghamshire, England).

In all cases at 120 °C, the eutectic showed the brownish discoloration. However, since the discoloration was lightest for the Fluka material, it was decided to use it when attempting to develop a standard purification technique.

Partial success in the purification of this material was seen in previous work after treatment of the final eutectic with Al turnings. The success was not complete, since the effectiveness of this treatment varied from case to case. We assumed that an aluminum oxide layer was responsible for the lack of consistency in the degree of purification, and attempted to solve this problem by using an amalgamated Al plate, which was kept under stirring in the eutectic for 6 hr. This treatment succeeded in removing the coloration and in substantially decreasing the iron peaks of the cyclic voltammetric curves. However, a small peak, introduced at a potential of about 1.5 V, can be attributed to the presence of Hg^{2+} in solution.

Pre-electrolysis of the eutectic at 120 °C for 24 hr, using Ultra Carbon U-5 grade carbon electrodes, was successful in decreasing the iron peaks, but did not improve the coloration sufficiently.

After these preliminary purification attempts, the following procedure was found to yield satisfactory results. $AlCl_3$ (Fluka) was mixed with NaCl and KCl in the ratio of about 1.0 mol KCl, 1.5 mol NaCl, and 9.8 mol $AlCl_3$, giving a liquid at ~130 °C with a high $AlCl_3$ vapor pressure. This liquid was treated with magnesium turnings to ensure the precipitation of such impurities as iron chloride, which show an appreciable vapor pressure. From this melt, $AlCl_3$ was evaporated at a constant temperature of 215 °C and condensed as large crystals in the cold part of the apparatus. By using two 1-l resin reaction kettles, as shown in Fig. 6, about 70 g of pure $AlCl_3$ was obtained overnight. Fig. 7 shows the crystallized material in the upper (cold) part of the apparatus. The material seems to be clean, as evidenced by its clearness, the production of virtually transparent eutectics, and the lack of any residual cur-

Fig. 6. $AlCl_3$ purification unit (in inert atmosphere chamber)

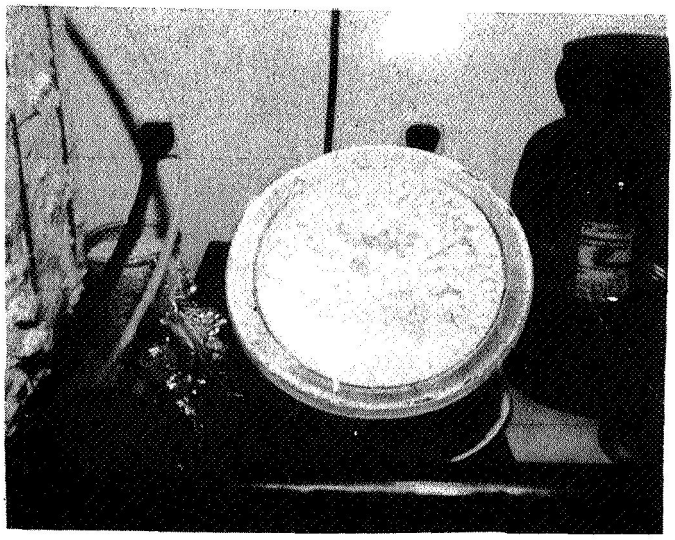

Fig. 7. View of condensed $AlCl_3$ crystals in cold part of purification unit

rent in the cyclic voltammetric curves obtained with the above eutectics.

This purification procedure used in the initial part of our investigations (Ref. 24) was later modified as follows. A quartz rack containing three electrodes (an Al wire in the center, an Al sheet cylinder as counterelectrode, and a Pt wire electrode) and a baffle was introduced into a 2-l kettle, which was surrounded by a heating mantle and which contained a Teflon-coated, magnetic stirring bar. A 1500-g salt mixture of $AlCl_3$-KCl-NaCl (67.5-13.38-19.12 wt %) was introduced into the vessel. Between 130 and 140 °C, the resulting melt had only a moderate $AlCl_3$ vapor pressure.

By using a high current (~10 A) between the Al electrodes, dendrites were formed at the wire electrode and partially separated from the electrode upon current reversal. Thus, high surface Al was produced in situ. The melt was kept under constant stirring at 140 °C for 24 to 36 hr.

The progress of the exchange of Fe^{3+} for Al^{3+} was monitored by cyclic potential sweeps at the Pt wire electrode. A reduction in the ionic iron by more than a factor of 25 was obtained. This procedure was then followed by raising the temperature and evaporating the $AlCl_3$ into an aircooled, 1-l reaction kettle placed upside down on top of the reaction vessel, as described above.

To determine qualitatively the effect of moisture, humidified argon was bubbled through the melt for a short period. It was observed that clouds of HCl gas were formed, and a thin

white deposit was left on the upper parts of the cell. No precipitate could be observed forming in the electrolyte. According to Letisse and Tremillon (Ref. 25), the reaction between H_2O and the equimolar $NaCl-AlCl_3$ is as follows:

$$2\ AlCl_4^- + H_2O \rightarrow 2\ HCl + Al_2OCl_5^- + Cl^-$$

It is presumed that a similar, if not identical, reaction occurs in the ternary eutectic.

Conductivity Measurements in $AlCl_3$-KCl-NaCl

Experimental. -- For these measurements, we designed a capillary conductivity cell (shown schematically in Fig. 8), made out of Pyrex glass with platinized platinum electrodes. This was mounted in a test-tube-like vessel containing a side arm for the connection to the pressure-controlled argon atmosphere. To ensure a uniform melt composition in the measuring capillary and in the remaining part of the vessel, the melt was mixed by forcing it out of the measuring section by a short application of positive argon pressure to the center tube of the cell before each measurement. Temperature was determined by a thermocouple directly at the capillary (see Fig. 8). The whole arrangement was heated by a stirred silicone oil bath controlled to ±0.2 °C by a Matheson Lab Stat in conjunction with a two-stage heater. The assembling of the cell and handling of the melt were performed in the argon atmosphere of the dry box. The cell resistance was measured by a precision ac bridge.

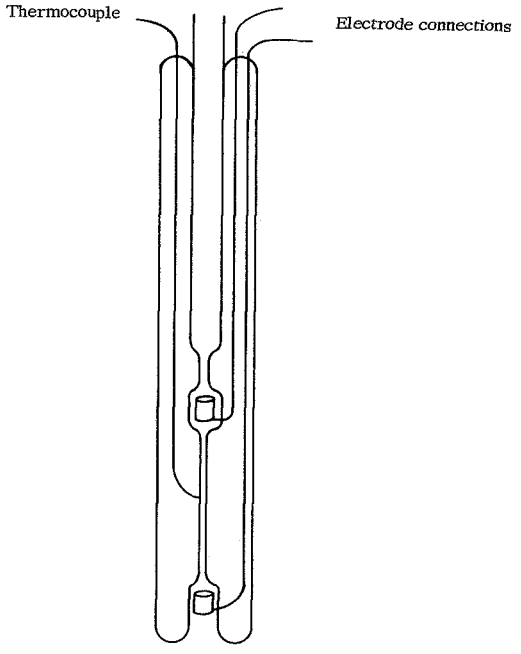

Fig. 8. Pyrex capillary conductivity cell

Results. -- The specific conductivity, κ_{sp}, is given by

$$\kappa_{sp} = \frac{a}{R} \ (\text{ohm}^{-1}\text{cm}^{-1})$$

where a is the cell constant and R is the measured resistance. The cell constant was determined in the standard way by using 1N KCl solution and the tabulated values for its conductivity (it was found to be 119.24 cm^{-1}). Generally, we used a measuring frequency of 1 kHz after establishing that the measured resistance values were independent of the ac frequency used (100 Hz to 10 kHz).

Table II shows the measured resistances and the specific conductivities of the $AlCl_3$-KCl-NaCl melt (57.5-12.5-30 mol %) which was used in many of our electrochemical in-

TABLE II

SPECIFIC CONDUCTIVITY OF $AlCl_3$-KCl-NaCl (57.5-12.5-30 MOL %)

Temperature, °C	Resistivity, ohms	κ_{sp}, $ohm^{-1}cm^{-1}$
131.7	678	0.1758
131.7	681	0.1751
128.2	715	0.1667
127.8	715	0.1667
133.9	765	0.1766
133.9	672	0.1774
134.6	668	0.1785
135.0	662	0.1801
139.9	633	0.1883
140.6	625	0.1907
141.0	625	0.1907
144.6	605	0.1970
145.3	594	0.2007
149.4	577	0.2066
150.4	569	0.2095
150.4	568	0.2099
150.6	565	0.2110
156.0	541	0.2204
156.5	537	0.2220
157.4	515	0.2315
161.8	511	0.2333
166.8	490	0.2433
167.0	488	0.2443
172.5	468	0.2547
172.7	466	0.2558
178.3	446	0.2673
178.9	444	0.2685
183.2	432	0.2760
183.5	428	0.2786
142.2	641	0.1860
132.2	669	0.1782
131.2	680	0.1753
130.1	681	0.1751

vestigations. Fig. 9 shows the temperature dependence of the conductivity data in an Arrhenius plot. These data can be represented very well by a straight line. A least squares fit leads to:

$$\kappa_{sp} = 11.4 \pm 0.9 \exp\left(-\frac{3360 \pm 68}{RT}\right) \qquad (125 \text{ to } 185\ ^\circ\text{C})$$

where the given range represents the 95% confidence limits.

Attempts are frequently made to relate the apparent activation energy obtained in this way to energy and entropy changes of postulated unimolecular rate processes. However, such a treatment would neglect changes in density, and thus the spacings, of the salt with temperature. Nevertheless, the equation represents a very good interpolation formula within the temperature range of our data.

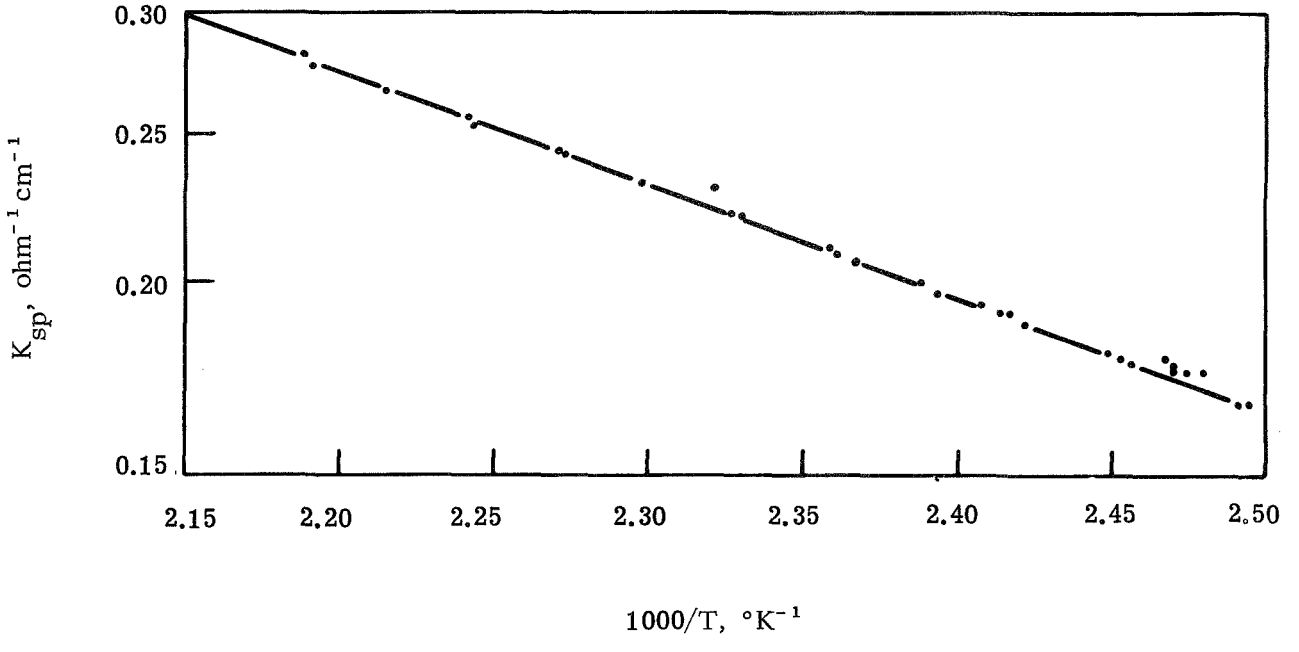

Fig. 9. Arrhenius plot of the specific conductivity of $AlCl_3$-KCl-NaCl (57.5-12.5-30 mol %)

Stationary, Partially Immersed, Carbon Electrodes

Experimental cell. -- The cell was a small (100-cc capacity), four-neck flask. The size was chosen in order to use small amounts of highly purified eutectic. The cell was operated in a hot air oven, and temperature control was ±1 °C at 120 °C. The oven was modified to allow for electrical connections to the various electrodes and to provide for argon and Cl_2 gas inlets and outlets (Fig. 10 is a photograph of the cell arrangement).

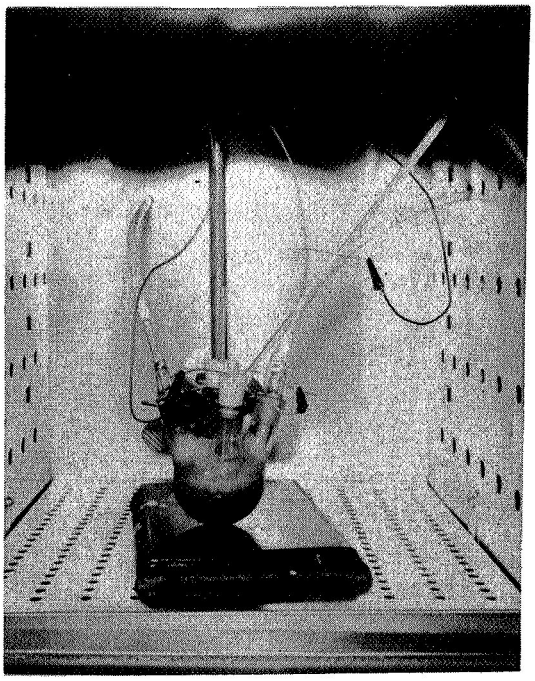

Fig. 10. Experimental cell in oven

Stability of carbon electrodes. -- Preliminary investigations using graphite (Speer Carbon Products grade 37-G electrographite) revealed that the electrolyte wets the porous graphite quite readily, and in a short period of time considerable swelling of the electrode was noticed (see Fig. 11). Upon removing the electrode from the melt, it was apparent that the graphite had lost its structural integrity. This behavior is in contrast to that observed by Swinkels (Ref. 26), where the same graphite electrode was not wet by molten LiCl at 650 °C.

Disintegration of the graphite seems to be a consequence of interplanar reactions resulting in the formation of intercalation compounds. Since the attack is even more pronounced in the presence of chlorine, the compatibility of carbon electrodes, from different sources and of different degrees of graphitization and porosity with respect to $AlCl_3$ eutectics, was studied

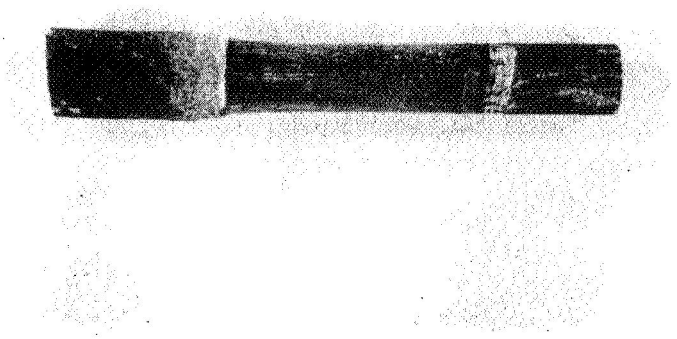

Fig. 11. Graphite electrode after immersion in melt for 2 hr (Speer graphite, grade 37-6; density = 1.35 g/cc; total porosity = 0.273 cc/g)

in the presence and the absence of chlorine. For these experiments, an $AlCl_3$-KCl-NaCl eutectic (66-14-20 mol %) at 120 °C was used. When investigating the effect of chlorine, the carbon electrode was partially immersed in the electrolyte, and chlorine was passed through the gas phase of the all-glass cell. The results of these experiments are presented in Table III.

This table shows that deterioration, as evidenced by the swelling or erosion of the surface, is much more evident in the presence of chlorine. Only in the case of a few graphite samples did substantial swelling occur in the absence of chlorine. Furthermore, corrosion by chlorine is very much more pronounced in samples with some graphite content than in carbon samples without graphite. The samples which resisted corrosion were a Pure Carbon PO2 sample, which is a high density carbon, and a Speer carbon sample (no. 37), which is a porous carbon with little graphite content. Vitreous carbon from Atomergic Chemetals did not show any deterioration, even after observation of the interface under the microscope. It also seems possible that pyrolytic graphite may show sufficient compatibility with the $Cl_2/AlCl_3$-eutectic environment. As a consequence of this work, we used the no. 37 Speer carbon material to determine the feasibility of a carbon-based, chlorine diffusion electrode, and Pure Carbon PO2 as construction material when a high density, impermeable carbon was required. Vitreous carbon is suitable for kinetic studies of chlorine reduction on smooth carbon surfaces. Some preliminary results are described in the following section.

Reduction of chlorine on smooth, vitreous carbon electrodes. -- We investigated the intrinsic activity of pure vitreous carbon for chlorine reduction in the $AlCl_3$-KCl-NaCl (66-14-20 mol %) eutectic melt with partially immersed, smooth electrodes. The meniscus is representative of

TABLE III

STABILITY OF CARBON-GRAPHITE MATERIALS IN $AlCl_3$-NaCl-KCl EUTECTIC IN THE ABSENCE AND PRESENCE OF CHLORINE

Material Identification	Source	Conditions: $AlCl_3$ Eutectic at 120 °C	Conditions: Cl_2 Passed Over Melt	Remarks on Cl_2 Effect
No. 37 porous carbon	Speer carbon	No attack	No attack	In contact over 48 hr
P-6038-C carbon-graphite	Pure carbon	↓	Failed	Failed in less than 15 min
PO2 dense carbon	Pure carbon	↓	No attack	
103G dense carbon	Speer carbon	↓	Failed	Failed in less than 10 min
104 dense graphite	↓	↓	↓	Same
108 dense carbon-graphite	↓	↓	↓	Same
37G porous graphite	↓	↓	↓	Same
Graphite "A"	Carborundum	Failed	↓	Rapid failure
L-50 porous carbon-graphite	Pure carbon	No attack	↓	Failure in 10 to 15 min
L-56 porous carbon-graphite	↓	↓	↓	↓
PO3 porous carbon-graphite	↓	↓	↓	↓
P3W porous carbon-graphite	↓	↓	↓	↓
CS grade dense graphite	National carbon	↓	↓	Failed in less than 30 min
Vitreous carbon	Atomergic Chemetals	↓	No attack	No attack after more than 72 hr contact with $AlCl_3$
Pyrolytic graphite	Ultra carbon			Pyrolytic graphite coating (a piece of plain graphite) appears to have resistance to attack

the three-phase boundary of a porous gas diffusion electrode (Ref. 27). For these experiments, a rod of vitreous carbon, 0.3-cm diameter from Atomergic Chemetals Corporation, was used. This carbon has a highly disordered structure which, coupled with a very high density, makes it very resistant to attack by chlorine in $AlCl_3$ eutectics. Another interesting feature of this material is its expansion coefficient, which allows us to make very good seals to borosilicate glass. The electrolyte was the $AlCl_3$-KCl-NaCl eutectic (unless otherwise stated) at a temperature of 120 °C. Al was used as both reference and counterelectrodes. The electrolyte was saturated with argon, and the chlorine gas was passed above the electrolyte level.

In an experiment with a half-immersed electrode 2 cm long, an open circuit potential of 2.1 V versus Al was obtained. Starting from this potential, the potentiostatic current-potential curve of Fig. 12 was obtained (each point was measured after waiting 5 min). To demonstrate that the current was produced by chlorine reduction on carbon, chlorine was replaced by argon, and the decay of current at constant potential was recorded as a function of time (Fig. 13). After renewed introduction of chlorine, the current increased again to a value close to the previous value. The delay in reaction to gas changes can easily be explained by the gas volume in the electrochemical cell and tubings. The effect of potential on current was further investigated, as shown in Fig. 14, by following the current as a function of time at constant potential.

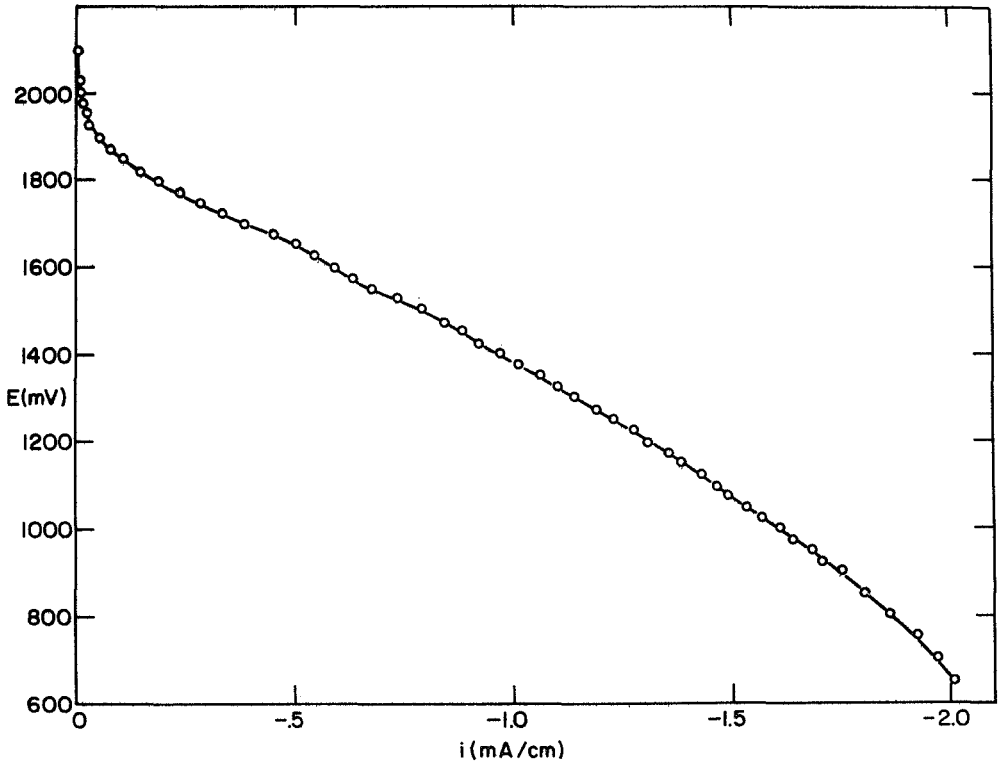

Fig. 12. Potentiostatic current-potential curve for Cl_2 reduction on partially immersed vitreous carbon electrode

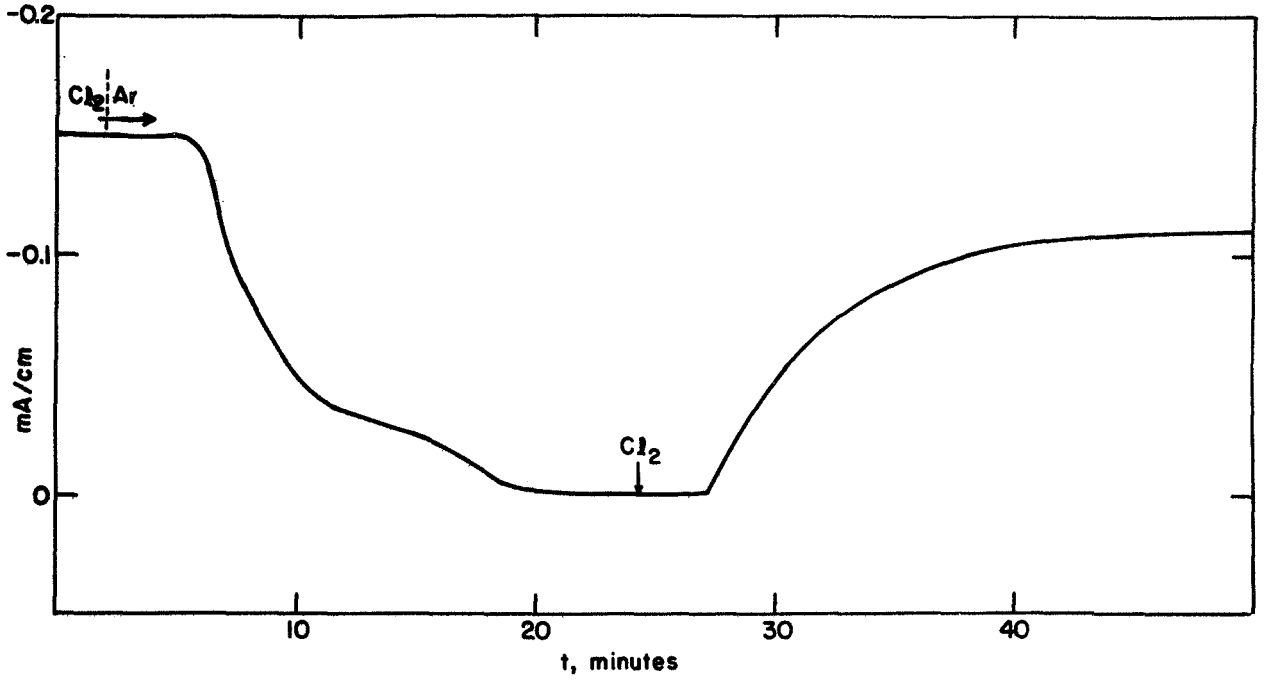

Fig. 13. Effect of Cl_2 gas on current obtained with partially immersed vitreous carbon electrode (potentiostated at 1.8 V versus Al reference electrode)

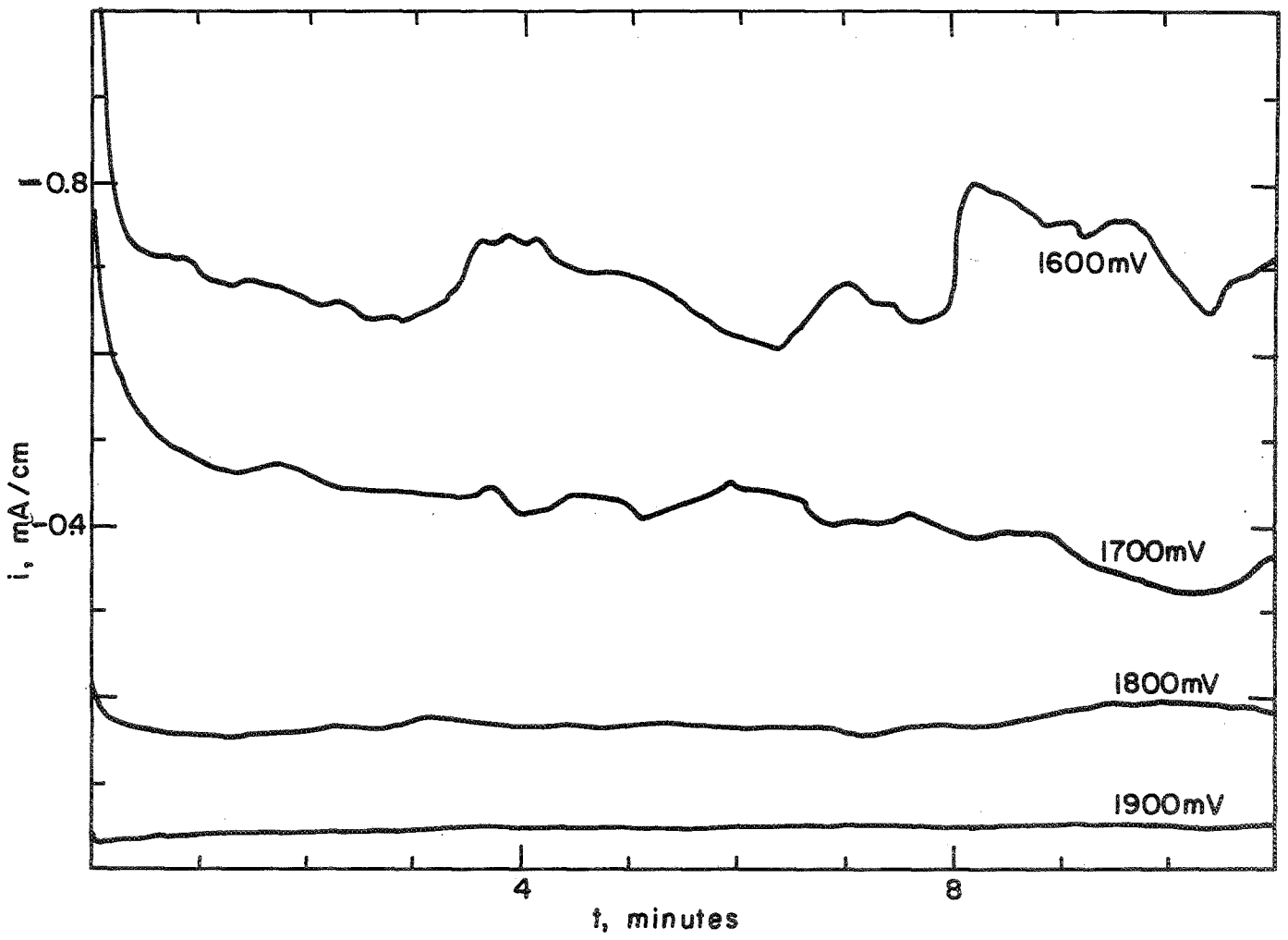

Fig. 14. Effect of potential on potentiostatic current-time curves for Cl_2 reduction on partially immersed vitreous carbon electrode

Fig. 14 shows that, although the currents are rather stable at the low polarizations, larger fluctuations occur at increasing polarizations. These are probably due to the effect of the increasing depth of penetration of chlorine reduction along the thin film with increasing polarization, and the resulting sensitivity to convection and to drying of the film.

In general, the results reported here can only be considered semiquantitative, since the film is not well defined due to the above mentioned changes caused by convection or drying. However, these results can be interpreted as clear proof that pure carbon is intrinsically active in catalyzing the reduction of Cl_2 in $AlCl_3$-KCl-NaCl electrolytes.

A series of tests was carried out to determine the contribution of the immersed part of the electrode in producing the current. In these experiments, the stagnant electrolyte had been saturated with chlorine. This did show that there was no decrease in current when the immersed part of the electrode was reduced practically to zero. Another series of experiments to establish approximately the effective length of the meniscus (and thin film) showed that reduction of the immersed part of the electrode down to 0.2 cm did not substantially affect the magnitude of the current.

In order to ascertain the effect of electrode pretreatment, the electrode was anodically polarized for 0.2 min, at a current density of +0.5 mA, to evolve chlorine. After this pretreatment, the activity for chlorine reduction of the carbon as a partially immersed electrode was substantially unchanged. The same was true after cathodically polarizing the electrode for 0.1 min at a 1000-mV potential.

In another experiment, the flow of chlorine was greatly increased above the electrolyte surface. This resulted in an increase of the current which could be attributed either to a drying of the film or to an increase of the chlorine partial pressure at the interface with the film. This experiment showed that, in order to use these types of data for quantitative measurements, extreme care should be taken in controlling the gas-phase concentration with respect to chlorine and $AlCl_3$ vapor.

To compare the activity of carbon with that of platinum, two experiments were carried out in the same melt and under the same conditions, first using a carbon electrode, and then a platinum electrode with the same degree of immersion. The results, given in Fig. 15, show that, overall, the activity of platinum is higher than carbon. The fact that the open circuit of the platinum electrode is about 60 mV lower than that of the carbon electrode can be construed as an indication of corrosion of the platinum electrode at the theoretical potential of the chlorine electrode.

Conclusions.--The work with partially immersed vitreous carbon electrodes indicates that carbon has enough intrinsic activity to warrant testing an unactivated porous carbon electrode as chlorine cathode in the $AlCl_3$-KCl-NaCl eutectic. In addition, the experience with vitreous carbon electrodes shows that this material should be ideally suited for studying the reduction kinetics of the dissolved chlorine using a rotating disk and a stationary electrode in pure $AlCl_3$

eutectics. Finally, the study of the compatibility of carbon materials for chlorine electrodes in $AlCl_3$ eutectics has uncovered carbon samples which appear suited for the construction of chlorine cathodes for operation in this electrolyte.

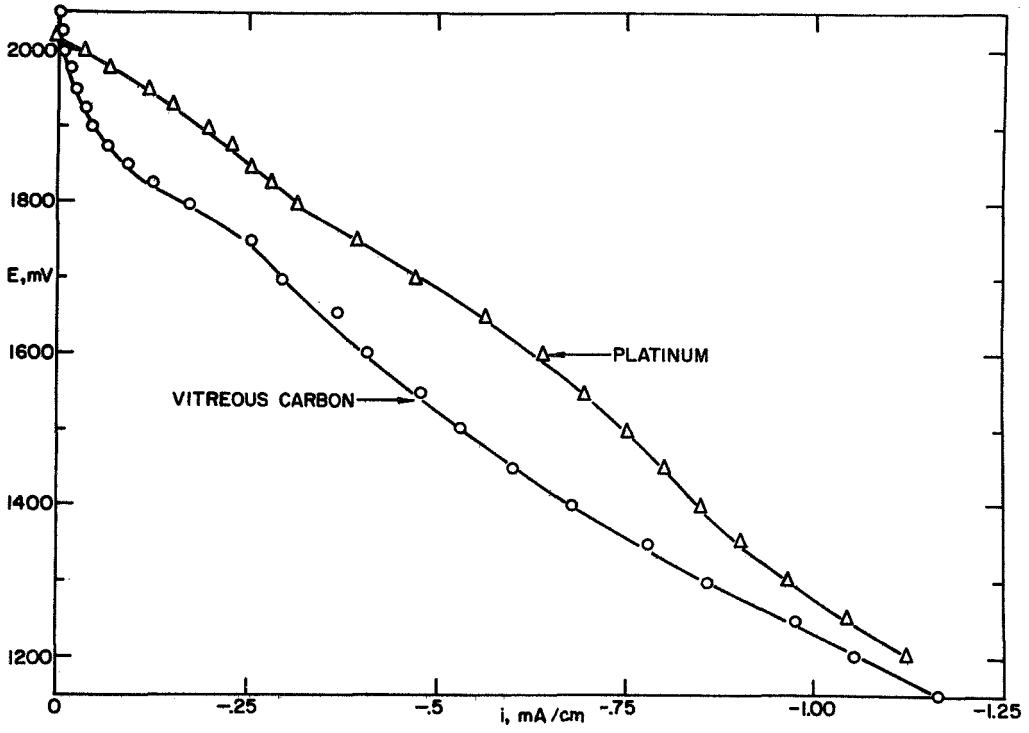

Fig. 15. Comparison of i-E curves for Cl_2 reduction on partially immersed platinum and vitreous carbon electrode

The Rotating Carbon Disk Electrode

Experimental. -- An overall view of the rotating disk electrode setup is shown in Fig. 16. It consisted of a sturdy stand on which a 1/15-hp Bodine motor and a precision ball bearing for the 0.25-in. rotating shaft were mounted. The motor speed was controlled by a Minarik speed control (SL-52). The coupling of the motor and the electrode shaft was accomplished by a non-slip belt. The rotation rate of the electrode was continuously monitored by the frequency modulation resulting from magnetic coupling of an electromagnet with an iron gear mounted on the rotating shaft. This signal was amplified and displayed on a frequency counter (Hewlett Packard model no. 5221A). Electrical contact to the disk electrode was accomplished through a mercury pool in the top of the rotating shaft.

The electrochemical cell was made of a 50-mm O-ring joint with a 30-mm-thick Teflon cover. The Teflon cover contained tapered holes to accommodate a liquid seal in the center with a 29/40 standard tapered joint surrounded by four 10/30 joints for the gas inlet and outlet as well as the counter- and reference electrodes. A Teflon bell was fixed to the rotating shaft (Fig. 17). Mercury and silicone oil with a very low vapor pressure were used as sealant liquids.

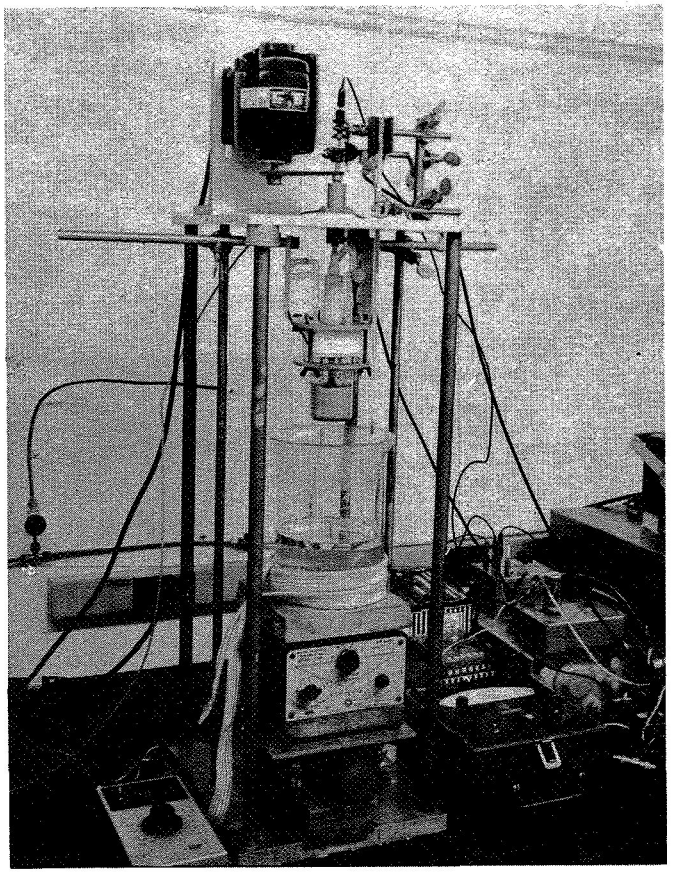

Fig. 16. Rotating disk electrode arrangement

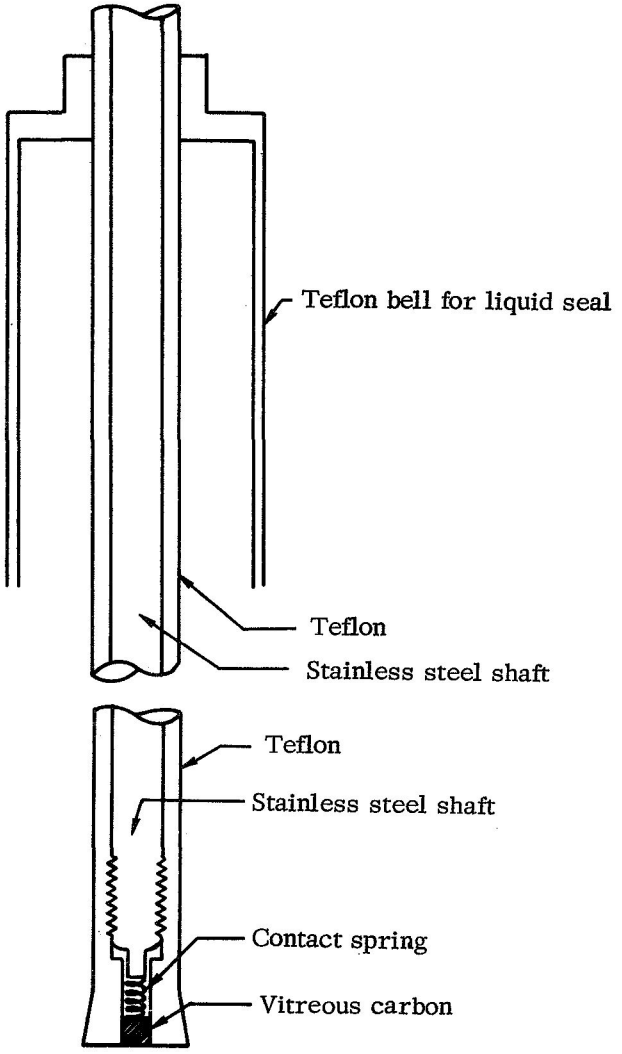

Fig. 17. Schematic diagram of rotating disk electrode

The rotating electrode consisted of a vitreous carbon rod (3-mm diameter, from Atomergic Chemetals Corp.) press-fitted into hot Teflon. Details of the electrode construction are shown in Fig. 17. A vitreous carbon rod was used as the counterelectrode. An Al electrode in the same melt, but in a separate compartment, served as the reference electrode.

The electrochemical cell was held at a constant temperature by a stirred silicone oil bath. Temperature was controlled to ±0.2 °C by a Matheson Lab Stat proportional temperature control unit and a two-stage heating arrangement.

The chlorine from a gas cylinder was passed through a trap filled with molecular sieves (Linde no. 5A) which had been dried at 375 °C under dry argon overnight before entering the cell.

Results. -- The experiments were conducted in the $AlCl_3$-KCl-NaCl melt (57.5-12.5-30 mol %) at 130 and 150.6 °C. Before introducing Cl_2 gas into the cell, cyclic voltammograms were taken at the carbon disk electrode (these showed practically no faradiaic background current). Following this, the argon was replaced by Cl_2, and a slow flow of Cl_2 gas was maintained above the melt surface. The progress of melt saturation with Cl_2 was monitored by measuring the increase of the limiting current of the Cl_2 reduction with time at constant rotation speeds. Generally, the stirred melt was saturated with Cl_2 after 25 to 30 min.

Current-potential relationship. -- The open circuit voltage was 2.10 V (versus Al) at 130 °C and 2.06 V at 150.6 °C. Typical current-voltage curves at 130 and 150.6 °C, at a sweep rate of 200 mV/min, are shown in Figs. 18 and 19. As can be seen from these figures, a slight hysteresis was observed between the forward and the backward sweep. The hysteresis at low current densities was practically independent of rotation rate, whereas the differences between the forward and backward sweeps at, or close to, the limiting current region increased with increasing rotation rate. Fig. 20 shows the change of current with time at constant potential at a rotation speed of 30 rps.

The initial current drop is due to the establishment of the concentration gradient in the diffusion layer, and will be of no concern in this context. This drop is followed by a relatively slow current decay which is clearly potential dependent. It is largest at 1.2 V, in keeping with the current-voltage curves (Figs. 18 and 19), and reaches a steady value after about 3 min. At 0.8 and 1.6 V, the current reaches steady-state value after about 1.5 min. This, and the fact that the current-voltage curve can be exactly reproduced after returning to the open circuit voltage, suggest that the observed inhibition is not only time but also potential dependent.

The exact cause of this behavior is not yet known. However, it seems most likely that some melt impurity is involved. Possibly, there might be a connection between the $Fe^{2+} \rightleftharpoons Fe^{3+} + e^-$ reaction, since there are still traces of iron in the eutectic and this reaction does seem to take place in this potential region at the vitreous carbon electrode.

Limiting current. -- The limiting current at a rotating disk electrode for a reaction which is controlled only by mass transfer is given by Levich (Ref. 28):

$$i_L = (\text{constant})\ nFD^{2/3}\ \upsilon^{-1/6}\ \omega^{1/2}\ C_0 \qquad (3)$$

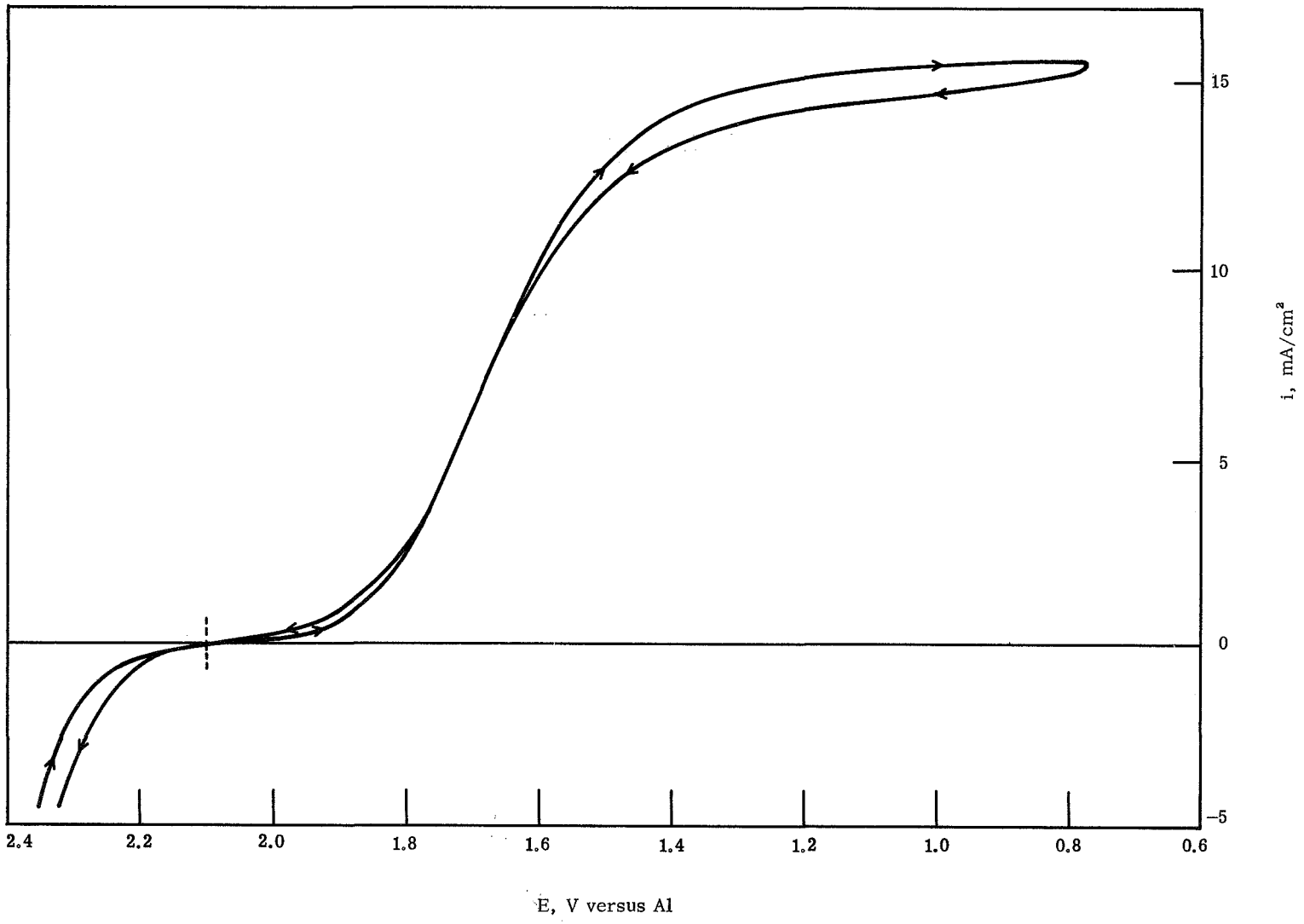

Fig. 18. Reduction of Cl_2 at rotating carbon disk electrode in $AlCl_3$-KCl-NaCl (57.5-12.5-30 mol %) at 130 °C, 20.8 rps, and 200 mV/min

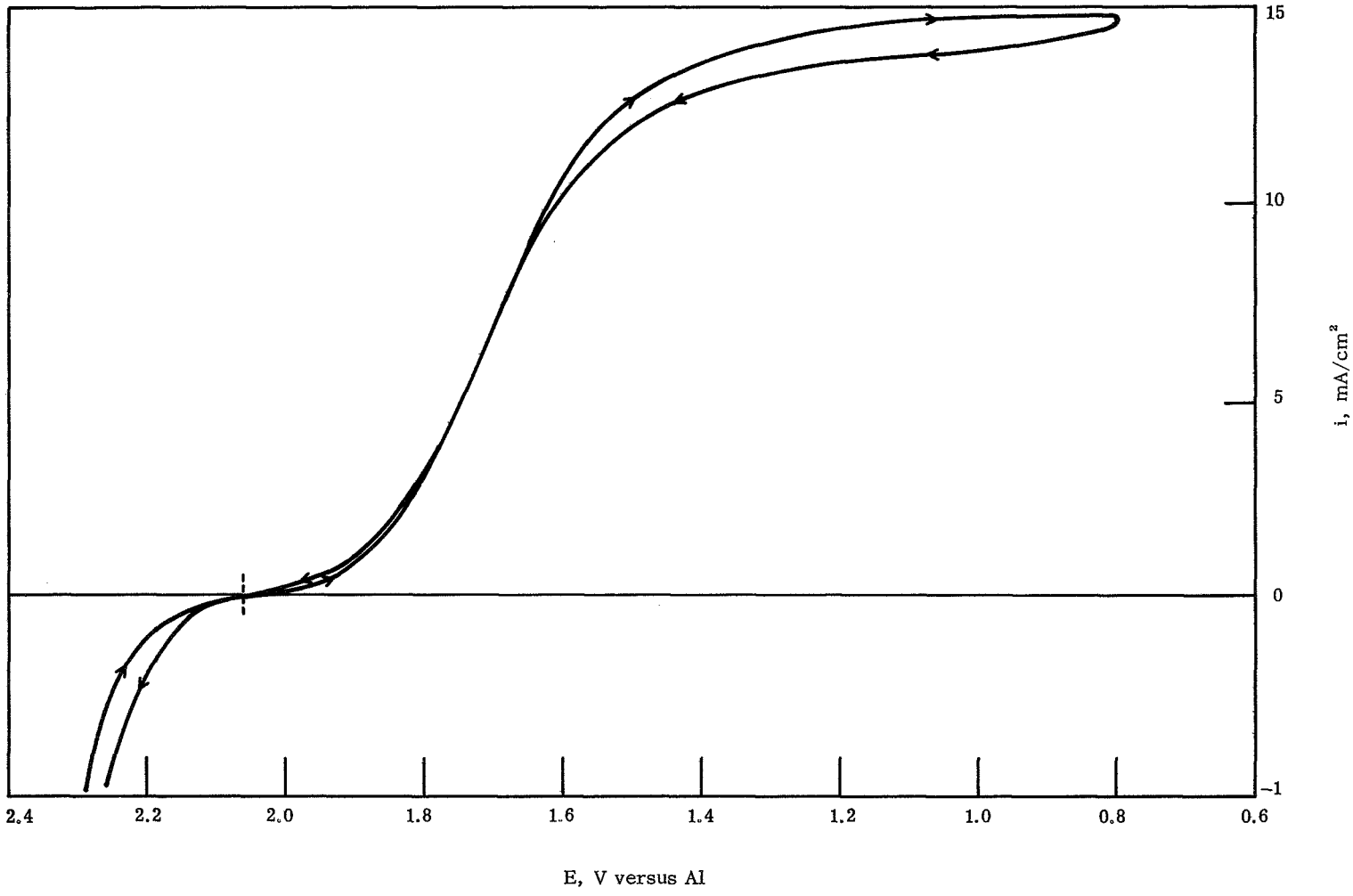

Fig. 19. Reduction of Cl_2 at rotating carbon disk electrode in $AlCl_3$-KCl-NaCl (57.5-12.5-30 mol %) at 150.6 °C, 30 rps, and 200 mV/min

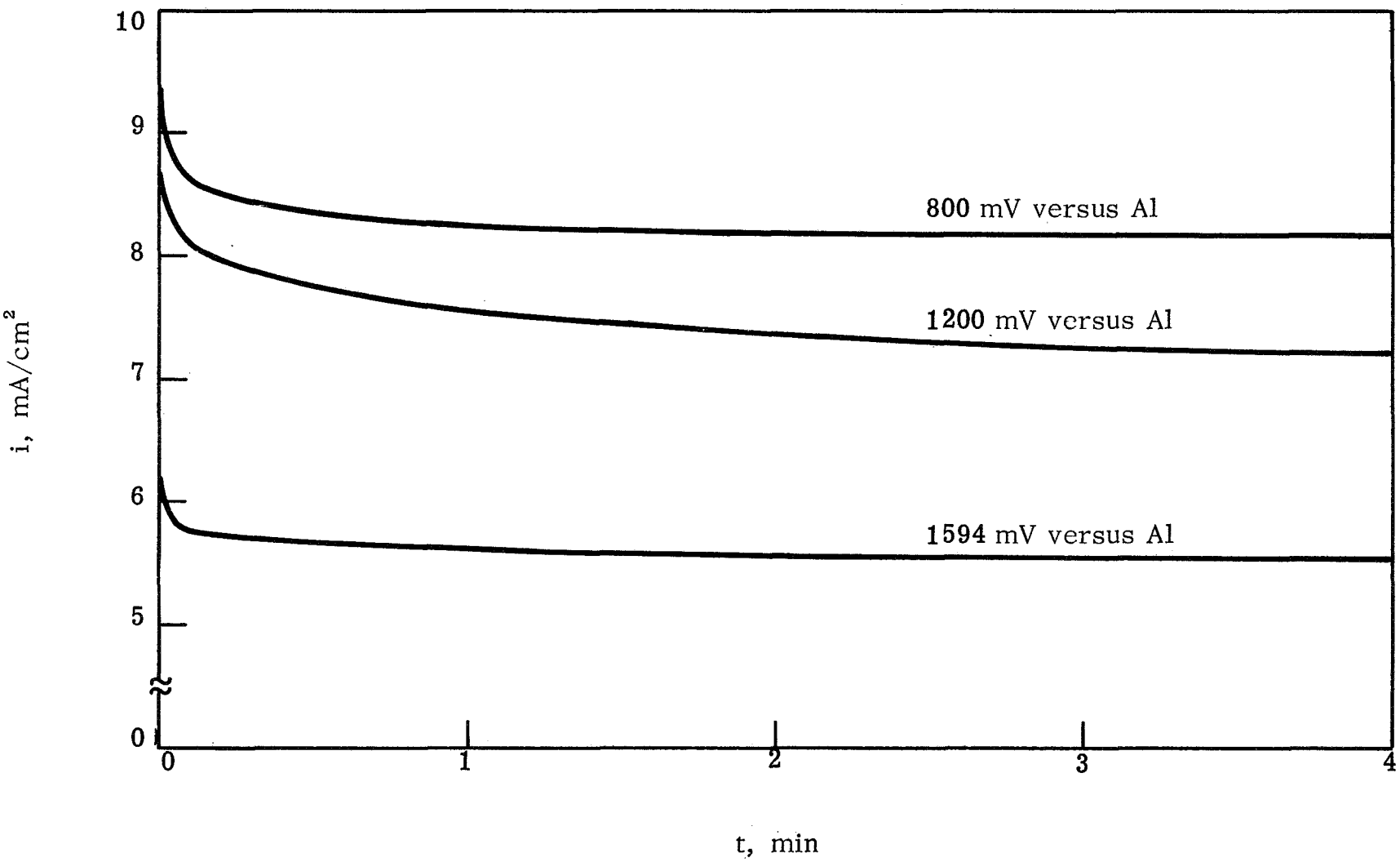

Fig. 20. Decay of Cl_2 reduction current with time upon potentiostatic steps to various potentials (versus Al) at the rotating disk electrode in $AlCl_3$-KCl-NaCl (57.5-12.5-30 mol %) at 130 °C and 30 rps

where the value of the constant is approximately 0.620, D is the diffusion coefficient, C_0 is the concentration of the electroactive species, υ is the viscosity, and $\omega = 2\pi$ (rps), rps = rotations per second. This equation implies a linear relationship between i_L and $\omega^{1/2}$ under diffusion controlled conditions. Fig. 21 shows such a plot for the reduction of Cl_2 at 130 and 150.6 °C. The limiting currents obtained from cyclic current-voltage sweeps at 3.3 V/min show a very good straight line with a slope of 1.48 mA/cm^2 $\omega^{1/2}$. The limiting currents from the slow current-voltage sweeps show a slightly larger scatter and a somewhat smaller slope (1.37 mA/cm^2 $\omega^{1/2}$), reflecting the slow current decay discussed earlier. At 150.6 °C, a slightly smaller limiting current was found, indicating that the increase in the factor $D^{2/3}$ $\upsilon^{-1/6}$ is overcompensated by the decrease of the Cl_2 solubility. From the slope of the plot in Fig. 21, one obtains, for the transport parameter ($D^{2/3}$ $\upsilon^{-1/6}$ C_0), approximately 1.4×10^{-8} at 130 °C.

An estimate of the diffusion coefficient and the solubility of Cl_2 can be obtained by comparing the limiting currents for Cl_2 reduction with those of another reaction, e.g., $Fe^{3+} \rightarrow Fe^{2+} + e^-$. We measured the limiting current of a Cl_2-free, $AlCl_3$-KCl-NaCl melt (57.5-12.5-30 mol %) containing approximately $5.3.\ 10^{-2}$ mol/l Fe^{3+} (an estimated value of 1.7 g/cm^3 was used for the density of the ternary melt). The limiting current was 2.8 mA/cm^2 $\omega^{1/2}$. Since υ will be on the order of 10^{-2} to 10^{-1} poise, one can calculate, from Eq. (3), a diffusion coefficient for Fe^{3+} of $\sim 1.5 \times 10^{-6}$ to 2×10^{-6} cm^2/sec. Thus, by assuming the same value for the diffusion coefficient of Cl_2, which might not necessarily be exactly correct since we are comparing a charged and an uncharged particle, we calculate a value of approximately 5.5×10^{-2} mol/l for the solubility of Cl_2 in our melt at 130 °C.

Kinetics of the Cl_2 electrode.--Clarification of the mechanism of the Cl_2 electrode is of great interest, since it will allow us to establish the rate-determining processes and eventually to suggest the best means to accelerate the reaction. In addition, the parameters which have to be determined to clarify the mechanism of the electrode reactions at a smooth electrode surface are parameters which have to be known to design rationally the best porous gas diffusion electrode structure (and eventually the best total system). The parameters of interest are: (1) exchange current, (2) order of reaction with respect to all possible species, (3) stoichiometric numbers, (4) transfer coefficient, α, (5) adsorption isotherms, and (6) activation energy.

One of the most widely used procedures to interpret polarization data is the use of Tafel plots:

$$\eta = a + b \log i \qquad (4)$$

where $a = \dfrac{2.3\,RT}{\alpha z F} \log i_0$

$$b = \frac{2.3\,RT}{\alpha z F}$$

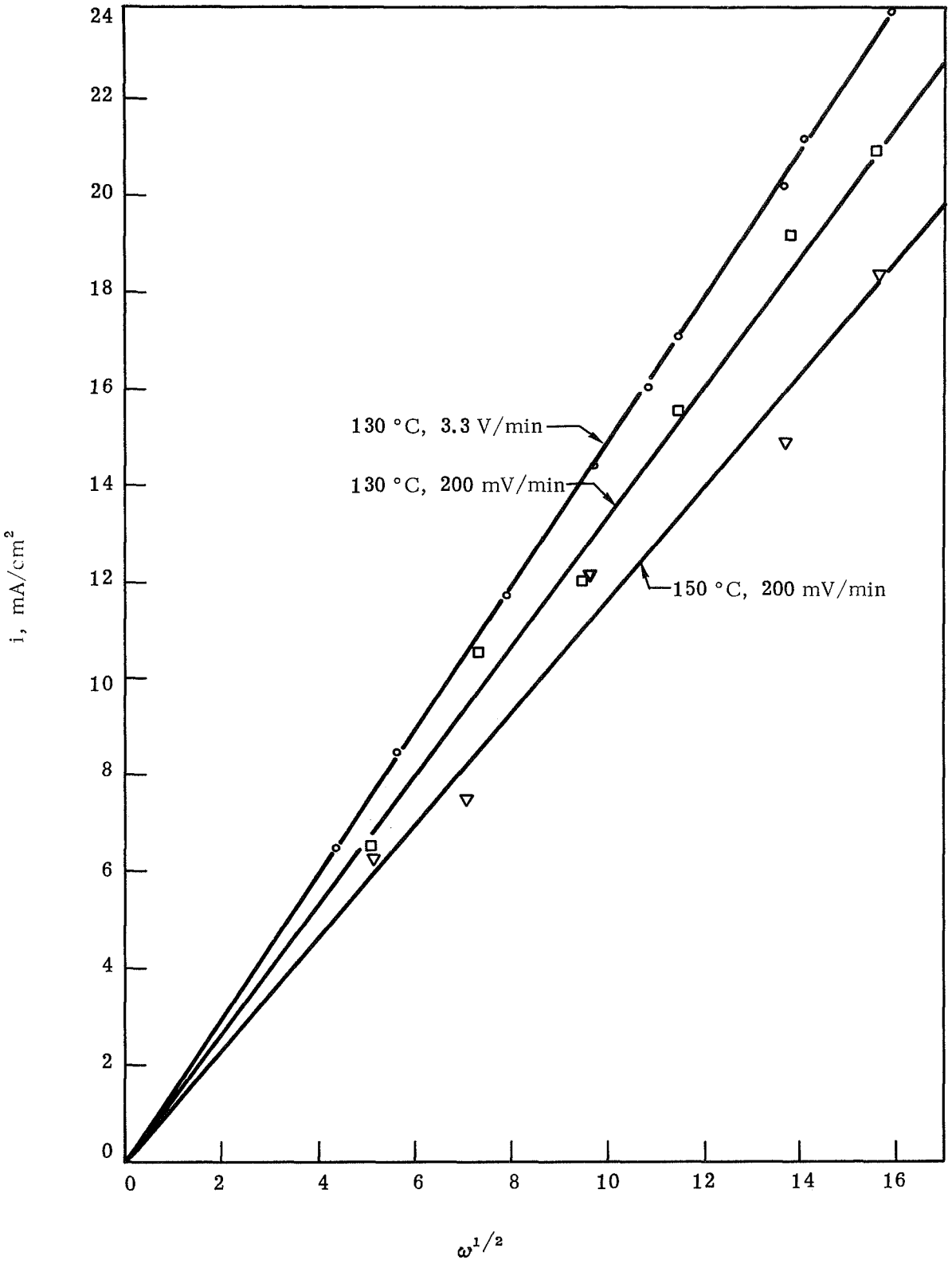

Fig. 21. Limiting currents for Cl_2 reduction versus rotation rate at carbon electrode in $AlCl_3$-KCl-NaCl (57.5-12.5-30 mol %)

The linear range of such a Tafel plot is often limited when applied to relatively fast reactions and/or when working with low concentrations. The region of linearity in a Tafel plot is reduced by the presence of diffusion limitations and the effect of the back reaction.

This difficulty can be circumvented when studying a single, rate-determining step reaction, with adsorption and of first order with respect to the diffusing species, by using the complete current-potential curve obtained with a rotating disk. For this, the current in the above equation must be replaced by i_{corr}:

$$i_{corr} = \frac{i}{[\, i - (i/i_{L,c})\,]\,[\, 1 - (i/i_{L,a})\,]\, \exp\,[\, (-zF/RT)\,\eta\,]} \qquad (5)$$

where $i_{L,c}$ and $i_{L,a}$ are the cathodic and anodic diffusion limited currents, respectively.

The $\log i_{corr}$ versus η plot is interpreted as usual Tafel plots, except that all the current-potential data are used instead of using only a small fraction. In our present case, $i/i_{L,a} \ll 1$, and the reaction is quite irreversible (thus the reverse reaction is negligible). Therefore, for the reduction of Cl_2, we have to consider the following equation:

$$\eta = \frac{2.3\,RT}{\beta zF} \log i_0 - \frac{2.3\,RT}{\beta zF} \log \frac{i}{1 - (i/i_{L,c})} \qquad (6)$$

where β is the symmetry factor for the cathodic reaction (which is not necessarily equal to $1 - \alpha$). A typical example of such a plot is shown in Fig. 22 in which the current-voltage curve of Fig. 18, at 130 °C, is plotted in a $\log i_{corr}$ versus η diagram according to the above equation. As can be seen from Fig. 22, the data show good Tafel behavior to overvoltages up to 500 mV. At higher overvoltages, deviations are noticeable. This is also the region where hysteresis between the forward and backward sweep was observed (compare Fig. 18). At lower overvoltages (between η = 50 and 250 mV), the current of the cathodic-going sweep seems to be too low, whereas the returning sweep follows the behavior predicted for a charge transfer reaction.

The exchange currents for the Cl_2 reduction determined from such plots were 1.0×10^{-4} A/cm^2 at 130 °C and 2.1×10^{-4} A/cm^2 at 150.6 °C. From an Arrhenius plot, one finds an activation energy for the exchange currents of 12 kcal/mol. The slope of the Tafel lines (compare Fig. 22) was found to be 200 mV at 130 °C and 210 mV at 150.6 °C. Thus, we obtain in both cases $z\beta = 0.4$, suggesting a one-electron transfer in the rate determining step.

As mentioned earlier, the extension of the Tafel plot according to Eq. (6) applies only to a rate-determining step of the type

$$O + z\,e^- \rightarrow R$$

i.e., to steps which are first order with respect to both components O and R. This is not always the case, and determination of the order of the reaction is indeed one of the most unequivocal ways of ascertaining the mechanism of an electrode reaction (Ref. 29).

If the rate-determining step is qth order with respect to a diffusing species, such as $qO = ze^- \rightarrow R$, the rotating disk electrode can be used with advantage to determine this order

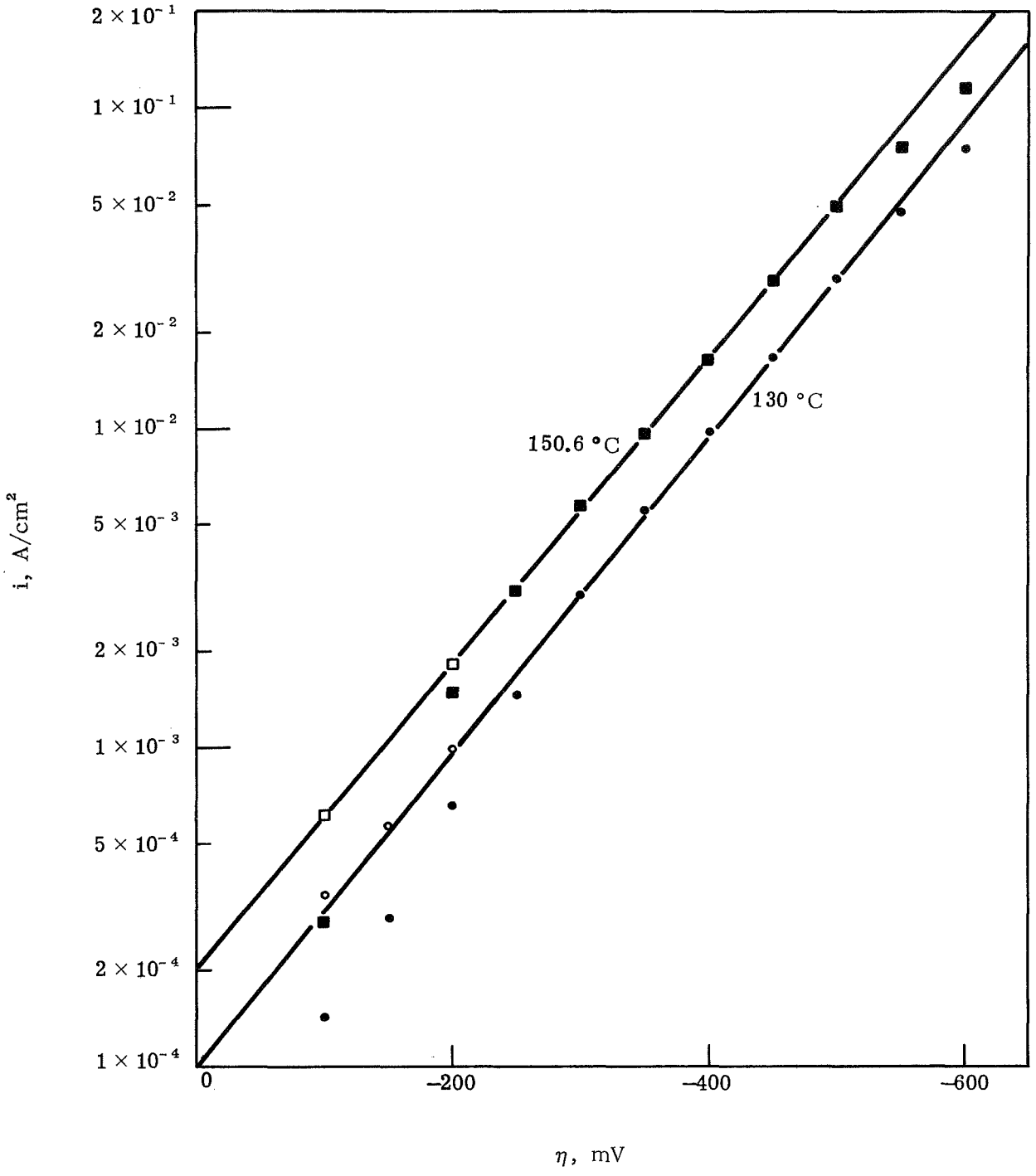

Fig. 22. Diffusion corrected Tafel plots of current-voltage curves shown in Figs. 18 and 19 (open symbols at low overvoltage represent returning sweep)

of reaction by studying the effect of rotation at a fixed potential at which the back reaction can be neglected. Under these conditions, we can write:

$$i = K (C_o^\circ)^q \tag{7}$$

and

$$i^* = K(C_o^\infty)^q \tag{8}$$

where i is the measured current (both activation and diffusion controlled), i* is the purely activation controlled current, and C_o^∞ and C_o° are the concentrations of species O in the bulk of the electrolyte and at the electrode surface, respectively.

Since

$$\frac{C_o^\circ}{C_o^\infty} = 1 - \frac{i}{i_{L,c}}$$

(where $i_{L,c}$ is the diffusion limiting current for the reduction of species O), one can write:

$$\frac{i}{i^*} = \left(1 - \frac{i}{i_{L,c}}\right)^q \tag{9}$$

A plot of log i versus log $[1 - (i/i_{L,c})]$ (obtained by varying ω) allows determination of both the value of q and i*.

When q = 1, Eq. (9) converts to

$$\frac{1}{i} = \frac{1}{i^*} + \frac{1}{K\omega^{1/2}} \tag{10}$$

When q = 1/2 (for instance), Eq. (9) converts to

$$i^2 = (i^*)^2 - \frac{(i^*)^2}{K} \frac{i}{\omega^{1/2}} \tag{11}$$

By plotting, for instance, 1/i versus $1/\omega^{1/2}$, or i^2 versus $i/\omega^{1/2}$, one can differentiate these two orders of reaction. This method was introduced by Frumkin and Aikazyan (Ref. 30). Two plots of log i versus log $(1 - i/i_{L,c})$ for 130 and 150.6 °C are shown in Figs. 23 and 24. The experimental points fall very nicely on a straight line with a slope of 1. There is also excellent agreement between the extrapolated currents, i*, and the Tafel plots of Fig. 22. Fig. 25 is a plot of 1/i versus $1/\omega^{1/2}$ according to Eq. (10). Again, the data points follow the predicted linear relationship. From the intercept at 1/i = 0, one may calculate i* = 80 μA/cm^2, as found in the Tafel plots. The slope 1/K = 780 cm$^2\omega^{1/2}$/A is in good agreement with K from the plot in Fig. 21.

Galvanostatic pulse measurements were used to determine the ohmic potential drop between the working electrode and the reference electrode. A typical value was 11 ohms at 130 °C. From the initial slope of the galvanostatic potential-time curve, the double layer capacity was

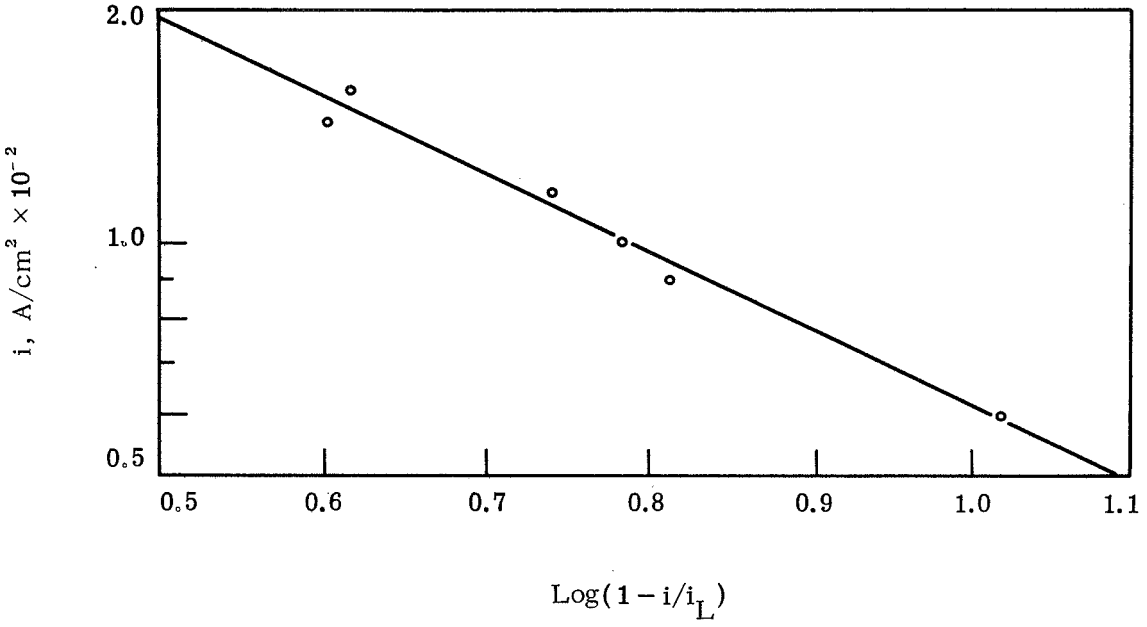

Fig. 23. Reduction of Cl_2 at constant potential (130 °C, E = 1.5 V versus Al, slope = 1.01, intercept = 78 mA/cm^2)

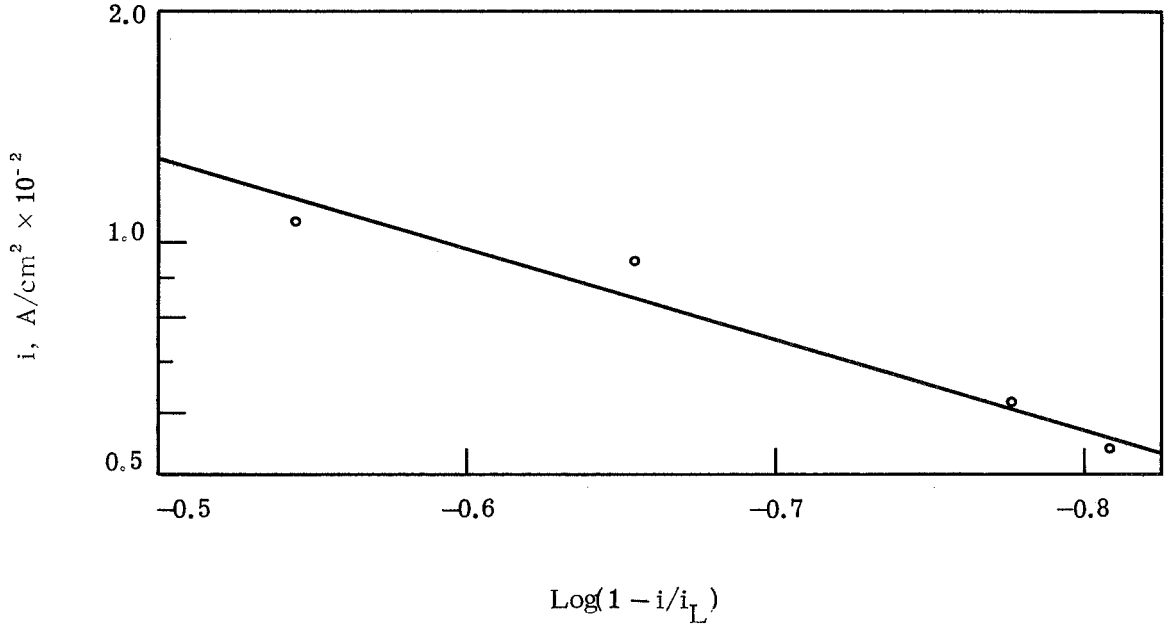

Fig. 24. Reduction of Cl_2 at constant potential (150.6 °C, E = 1.6 V versus Al, slope = 1.04, intercept = 50 mA/cm^2)

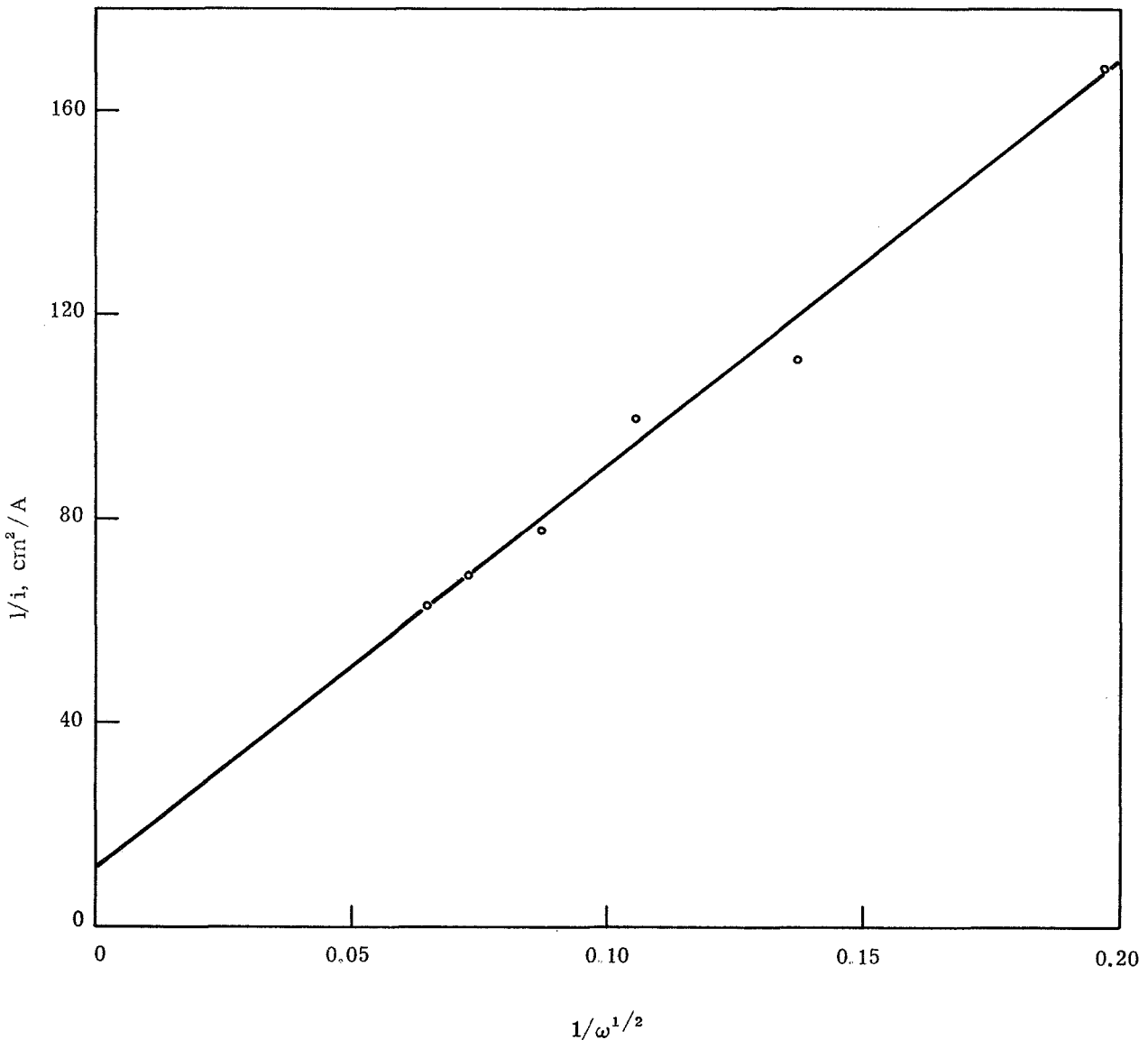

Fig. 25. Reduction of Cl_2 at constant potential (130 °C, E = 1.5 V versus Al)

calculated according to the equation:

$$C_d = i \frac{dt}{d\eta}$$

The experimentally determined capacity value was $C_d = 110 \pm 15\ \mu F/cm^2$, which is larger than the 20 to 30 $\mu F/cm^2$ one would normally expect to find. The larger capacity values might be due to an increased roughness factor of the electrode surface and/or an adsorption capacitance.

Discussion.--The overall reaction:

$$Cl_2 + 2\,e^- \rightleftharpoons 2\,Cl^-$$

can occur according to two paths:

$$1 \quad \begin{matrix} (a)\ Cl_2 + e^- \rightleftharpoons Cl^- + Cl \\ (b)\ Cl + e^- \rightleftharpoons Cl^- \end{matrix}$$

$$2 \quad \begin{matrix} (a)\ Cl_2 \rightleftharpoons 2\,Cl \\ (b)\ Cl + e^- \rightleftharpoons Cl^- \end{matrix}$$

The fact that the reaction for the chlorine reduction was found to be first order excludes the second path.

We can calculate the theoretical Tafel slopes of the first path, depending on whether step (a) or step (b) is rate determining, by following the simplified calculation of Fraser and Barradas (Ref. 31). It is based on the original treatment of Parsons (Ref. 32), and is applicable when low coverage Langmuir kinetic equations can be used and when the current does not depend on the potential of the Gouy-Helmholtz boundary of the double layer.

The cathodic Tafel slope can be obtained by

$$b_c = -\frac{RT}{F}\,[k + \beta\,(\ell - k + n/\upsilon)^{-1}$$

where n is the number of electrons in the overall reaction, υ is the number of times the rate-determining step occurs if the overall reaction occurs once, k is the number of electrons that must be taken from the electrode for the rate-determining step to occur once, $(-\ell)$ is the number of electrons which must be removed to permit the products formed by the occurrence of one rate-determining step to be transferred to the final state, and β is the symmetry factor for the cathodic reaction (in the following calculation, β is assumed to be 0.5):

Rate-Determining	n	υ	ℓ	k	b_c
1-a	2	1	–1	0	2 RT/F
1-b	2	1	0	1	2 RT/3F

In our experiments, the Tafel slope was found to be 2.5 RT/F, thus suggesting that the first path (step a) is the rate-determining step, with $\beta = 0.4$

The only work reported on the mechanisms of the chlorine electrode in molten $AlCl_3$-

alkali chloride electrolyte has been carried out by Skundin, et al. (Ref. 33), who have investigated the reduction of chlorine on Pt and Ir electrodes in the low melting eutectic, $AlCl_3$-KCl-NaCl, at 100 to 150 °C. The melt was saturated with Cl_2 (4mM at 110 °C), and linear voltammetric scans were applied at scan rates from 0.125 to 16 V sec^{-1}. The resulting peak-shaped current-voltage curves were recorded oscillographically. The reduction peak for Cl_2 at the Ir electrode was found to move in a more cathodic direction with increasing scan rate. This irreversible behavior allowed an estimate to be made of the exchange current density, which was of the order of 10^{-4} A/cm^2.

At Pt, the current-voltage curve for the reduction of Cl_2 had a markedly different shape. Two peaks were present, the more anodic of which was presumed to be due to direct Cl_2 reduction. The potential of this peak did not change with increasing scan rate, indicating that the electrode process was more reversible, i.e., faster than the corresponding one at Ir. The second peak was thought to be due to the reduction of Cl_2 complexed in some way with $AlCl_3$.

Analysis of the current-voltage data, in the form of Q versus $V^{1/2}$ plots, indicated the absence of any surface films on the Ir or Pt. However, galvanostatic measurements would have been useful in confirming this conclusion.

Investigations of the kinetics of Cl_2 reduction on carbon in $AlCl_3$-alkali chloride electrolyte are nonexistent. In aqueous solutions, for example, Frumkin and Tedoradse (Refs. 34 and 35) found that the rate-determining step for Cl_2 reduction at Pt electrodes was first order and involved electron transfer, thus suggesting a mechanism according to path 1. Contrary to this, Triaca, Solomons, and Bockris (Ref. 36) concluded from their investigations in molten LiCl (650 to 770 °C) at graphite electrodes that the chlorine reduction occurs according to path 2, with (a) being the slow step. This would suggest that the mechanism of Cl_2 reduction is different in molten $AlCl_3$-KCl-NaCl and LiCl. It should be mentioned, however, that Triaca, et al., used galvanostatic pulses and did not determine the reaction order. Further, they conceded in their paper that the estimation of the cathodic Tafel slope from their experiments was difficult.

THE ALUMINUM ELECTRODE

Experimental

An electrochemical cell was built using two O-ring joints with 50-mm inside diameter. An overall picture of the cell arrangement is given in Fig. 26.

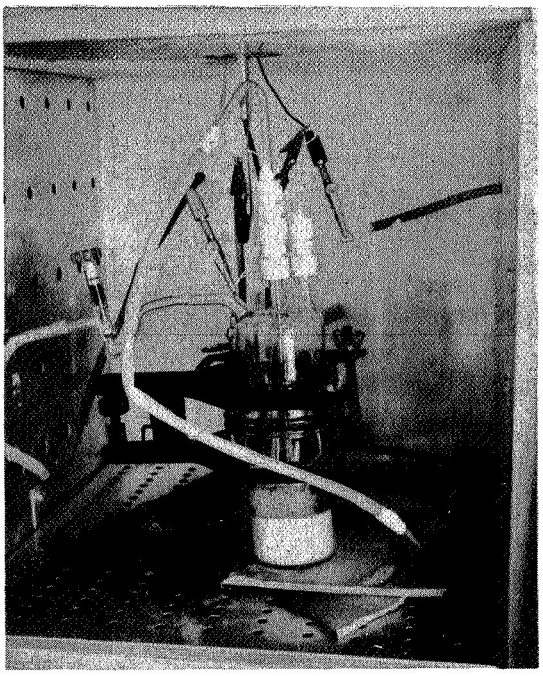

Fig. 26. Electrochemical cell

The cell top contained four tubes and a Teflon needle valve for the gas inlet and outlet and for the connections to the electrodes. A Viton O-ring was used as gasket. The electrodes and the gas inlet tube were connected with Teflon Swagelok fittings, using stainless steel back ferrules. The Al working electrode consisted of a pure Al wire 1.2 cm in length and 1 mm in diameter. The rest of the wire was covered with several layers of shrinkable Teflon. The reference electrode was also Al, and was contained in a separate compartment with a narrow opening to protect it from changes in electrolyte concentration. An Al wire wound in a spiral along the inside of the vessel served as counterelectrode. The cell also contained a platinum electrode sealed into glass for measurements of the electrolyte background.

The gas inlet part of the cell was connected to a tank of argon over a pressure control consisting of an electromagnetic valve and a mercury contact manometer. Thus, we could keep a constant, adjustable argon pressure (normally, a positive pressure of 10 to 20 torr was used). This arrangement also indicates immediately if there is a leakage in any of the cell joints.

For the experiments, the cell was filled and assembled tightly in the glove box, then transferred to the oven and connected to the argon line. The measurements were made with no gas passing through the cell to avoid concentration changes resulting from the appreciable vapor pressure of $AlCl_3$ over the melt.

The appearance of the melt was clear, but it turned grayish with time. There seemed to be a slight interaction between the melt and Teflon, resulting in a dark discoloration of the Teflon at the interface.

Results and Discussion

The experiments were conducted at different temperatures (157, 126, and 105 °C) and different $AlCl_3$-KCl-NaCl compositions (melt I: 67-13.6-19.4 mol %, melt II: 59-17-24 mol %, and melt III: 57.5-12.5-30 mol %). Melts I and II contained varying amounts of $AlCl_3$ at constant KCl/NaCl ratio. In terms of the phase diagram (Fig. 1), this means that the compositions are represented by points on a line through the compositions pure $AlCl_3$ and the ternary eutectic. Melt III lies approximately on the line from pure $AlCl_3$ to the pseudobinary eutectic between $NaAlCl_4$ and $KAlCl_4$. These melts promise to be more favorable for practical application than the composition of the ternary eutectic, since they stay liquid over a wider concentration range at temperatures around 130 °C.

The electrochemical measurements consisted of slow cathodic and anodic potential sweeps, recordings of current versus time at different preset cathodic and anodic potentials, and potential-time curves at constant current pulses. Typical current-potential and current-time curves for these results are shown in Figs. 27 through 35.

All current-potential and current-time curves show more or less pronounced passivation phenomena. Their dependence on charge passed through the electrode, on electrolyte composition, and on temperature will be discussed in detail in the following paragraphs.

Effect of Potential and Time

Anodic behavior. -- The anodic potential sweeps in Figs. 27 through 29 and 31 through 34 show that the anodic passivation of the Al electrode does not occur at a constant, defined potential. A closer examination reveals that it is not the potential but rather the charge (current and time) which is the parameter determining the sudden current drop. Fig. 29 shows the correlation between anodic passivation and cathodic prepolarization. Comparison of the anodic and cathodic charges (represented by the area underneath the i-t curve) shows that they are nearly equal. This is even more obvious from Fig. 30, which shows the cathodic and anodic currents versus time upon potentiostatic polarization to ±100 mV for periods of varying length. This behavior seems to indicate that melt I (which is $AlCl_3$-rich) cannot tolerate much more anodic formation of $AlCl_3$ without precipitating it as an insoluble passivating salt. On the other hand, if by cathodic pretreatment we form a diffusion layer close to the electrode which is poor in $AlCl_3$, then we are able to polarize the electrode anodically for a time necessary to replenish

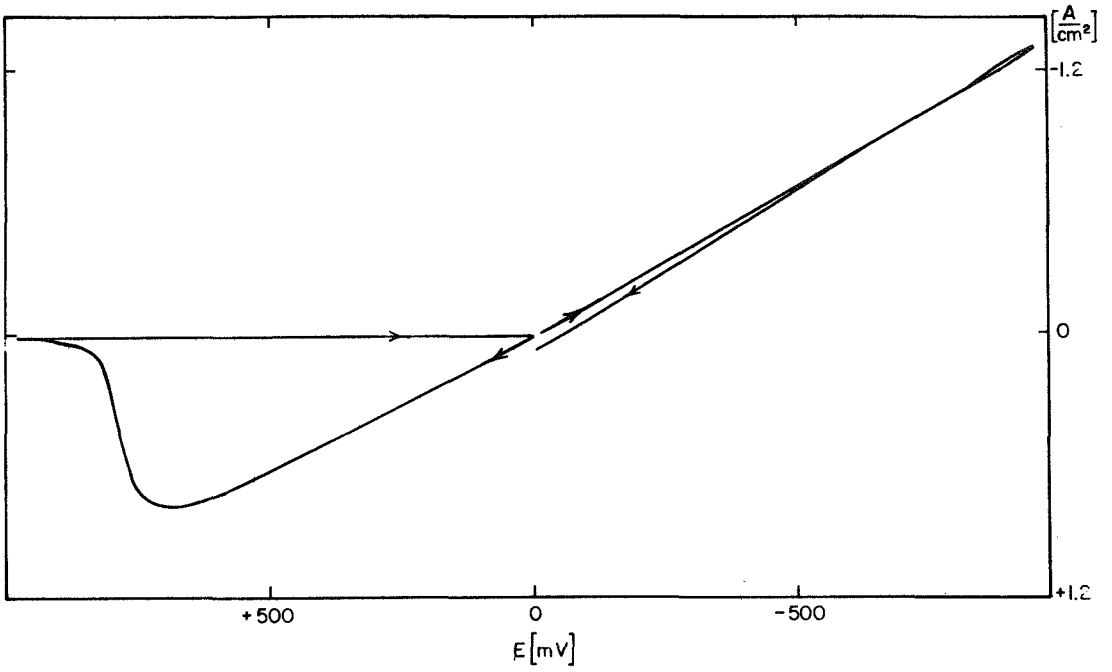

Fig. 27. Two triangular scans at Al electrode in melt I at 157 °C and 20 mV/sec (0 mV to +1 V back to 0 mV, and 0 mV to −1 V back to 0 mV; no i-R correction)

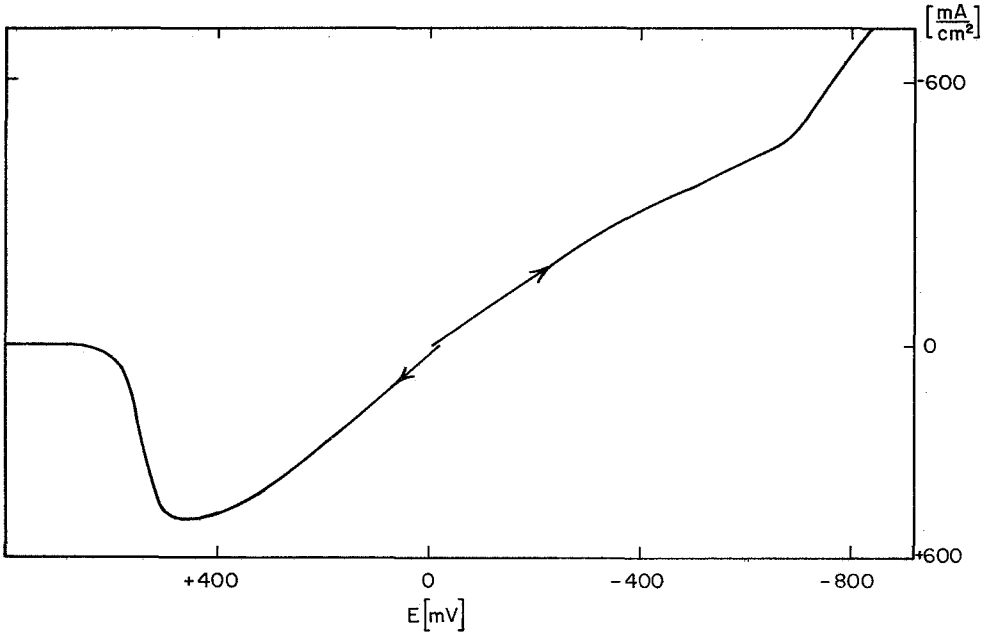

Fig. 28. Linear anodic and cathodic potential scans, starting from reversible potential, obtained at Al electrode in melt I at 115 °C and 400 mV/min (no i-R correction)

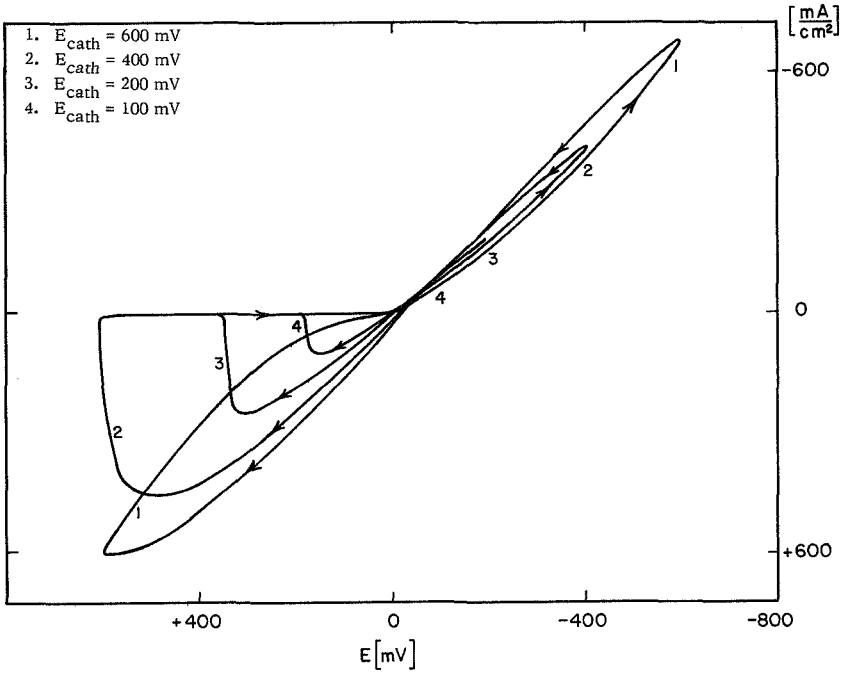

Fig. 29. Triangular potential scans at Al electrode in melt I at 105 °C and 400 mV/min (from 0 mV to E_{cath} to E_{anod} back to 0 mV; no i-R correction)

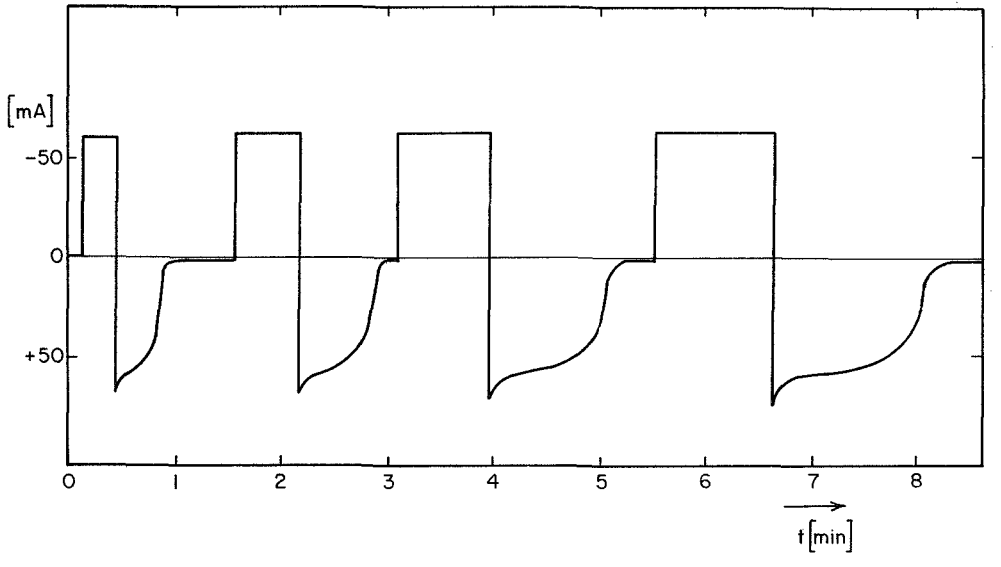

Fig. 30. Potentiostatic current-time curves at Al electrode in melt I at 156 °C (cathodic potential pulses of −100 mV and variable length followed by anodic pulses of +100 mV; no i-R correction)

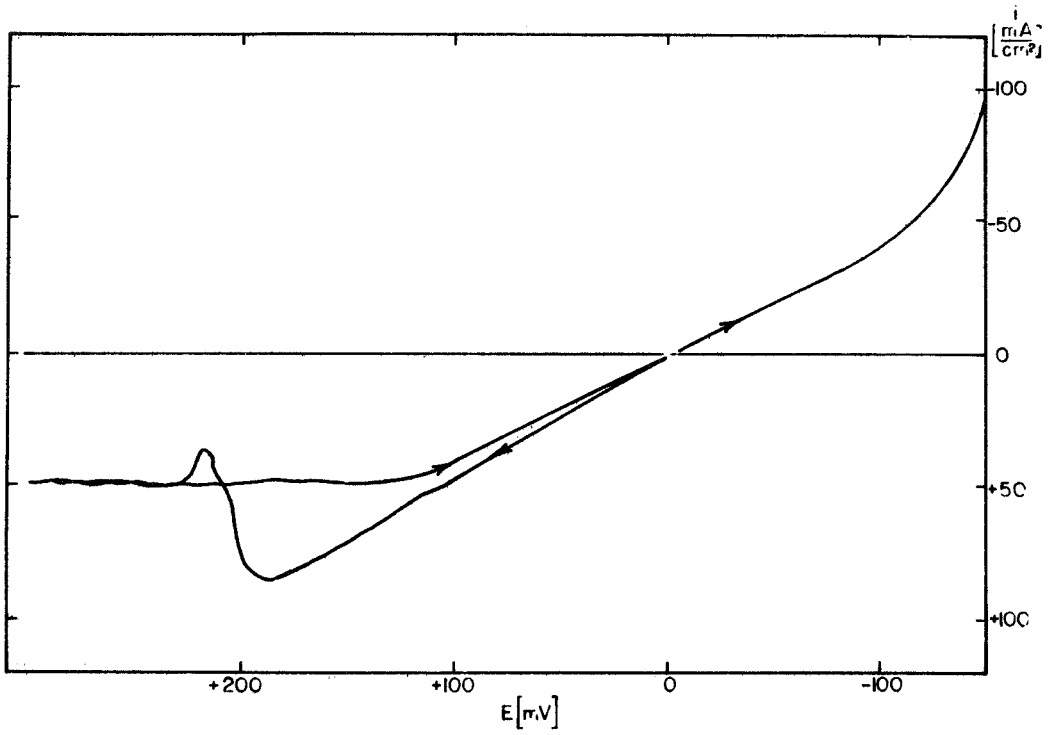

Fig. 31. Triangular anodic potential scan (0 mV to 300 mV back to 0 mV) and linear cathodic potential scan (0 mV to −150 mV) at Al electrode in melt II at 157 °C and 20 mV/min (no i-R correction)

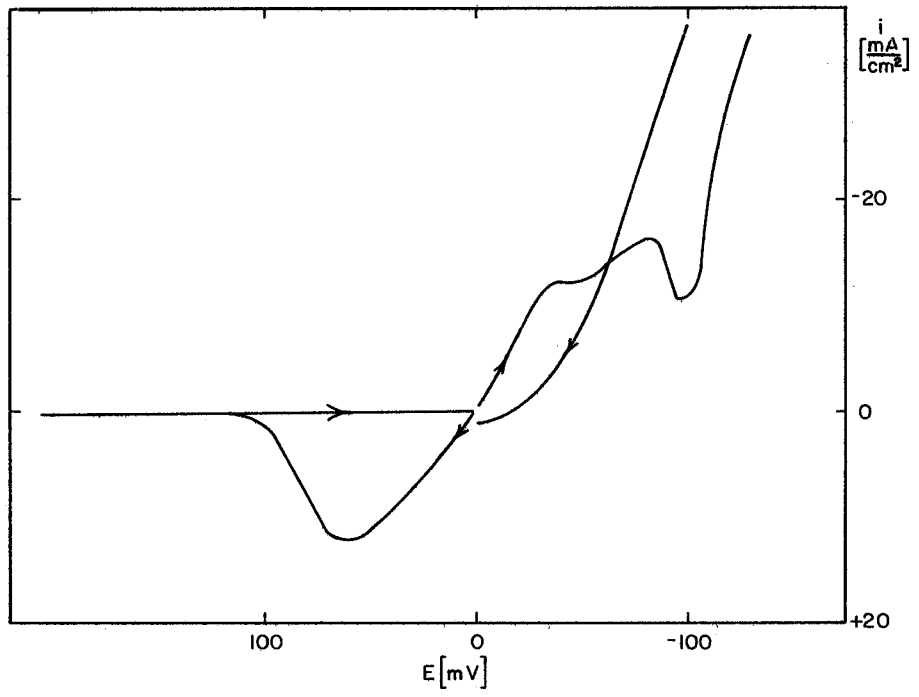

Fig. 32. Triangular cathodic potential scan (0 mV to −150 mV back to 0 mV) and anodic potential scan (0 mV to 200 mV back to 0 mV) at Al electrode in melt II at 105 °C and 20 mV/min (no i-R correction)

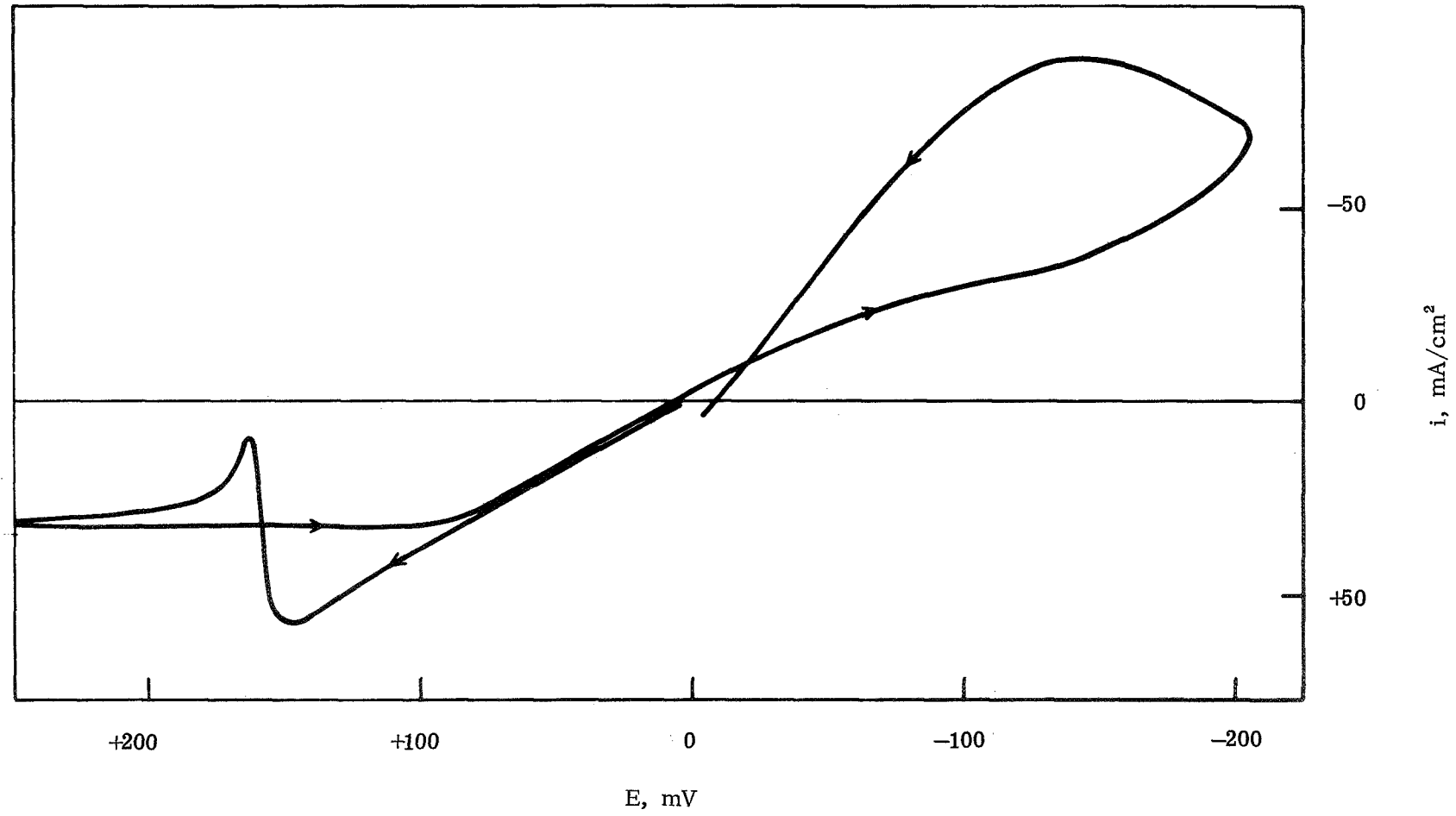

Fig. 33. Separate triangular anodic and cathodic potential scan at Al electrode in $AlCl_3$-KCl-NaCl (57.5-12.5-30 mol %) at 126 °C, 20 mV/min (no i-R correction)

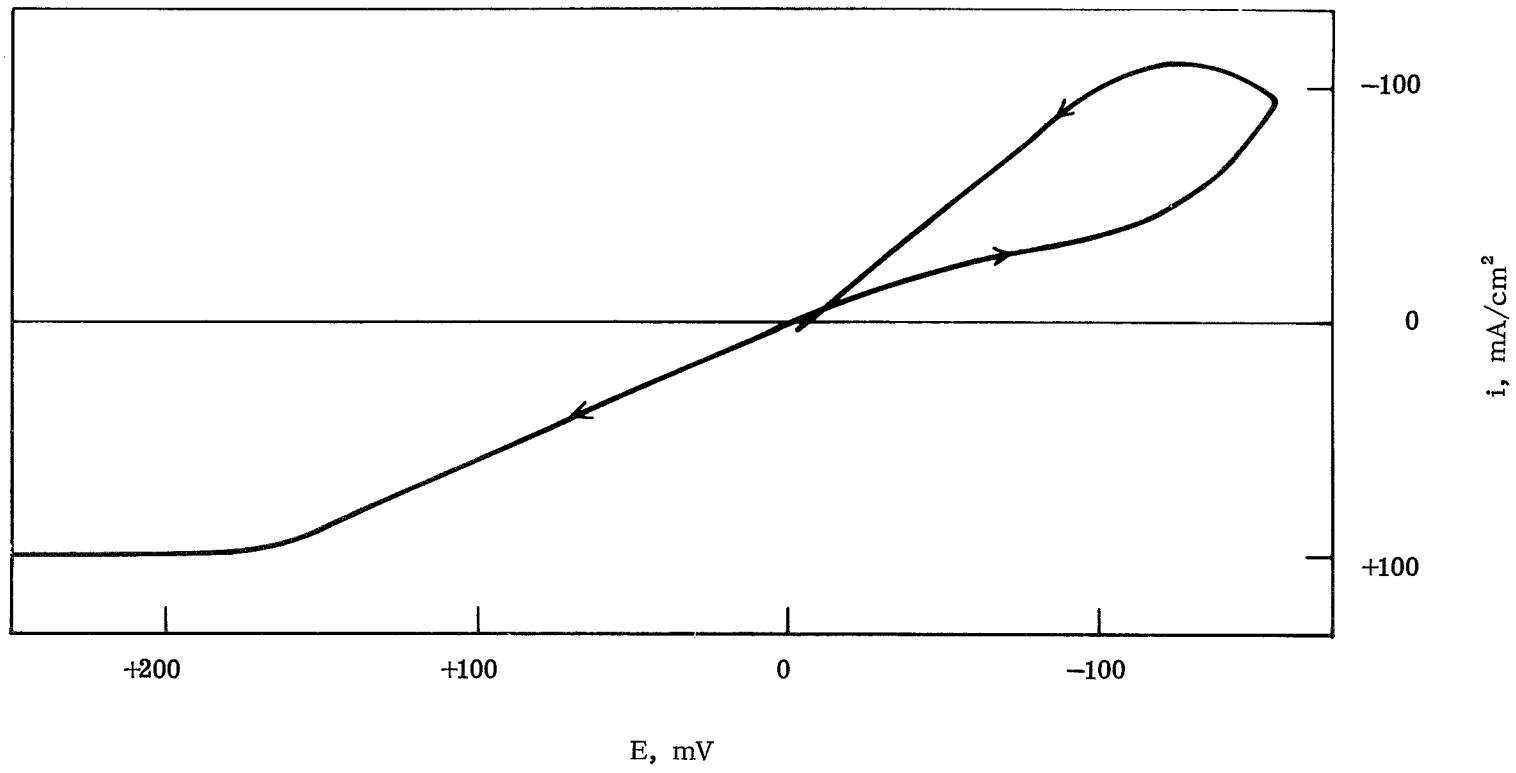

Fig. 34. Separate triangular anodic and cathodic potential scan at Al electrode in $AlCl_3$-KCl-NaCl (57.5-12.5-30 mol %) at 157 °C, 20 mV/min (no i-R correction)

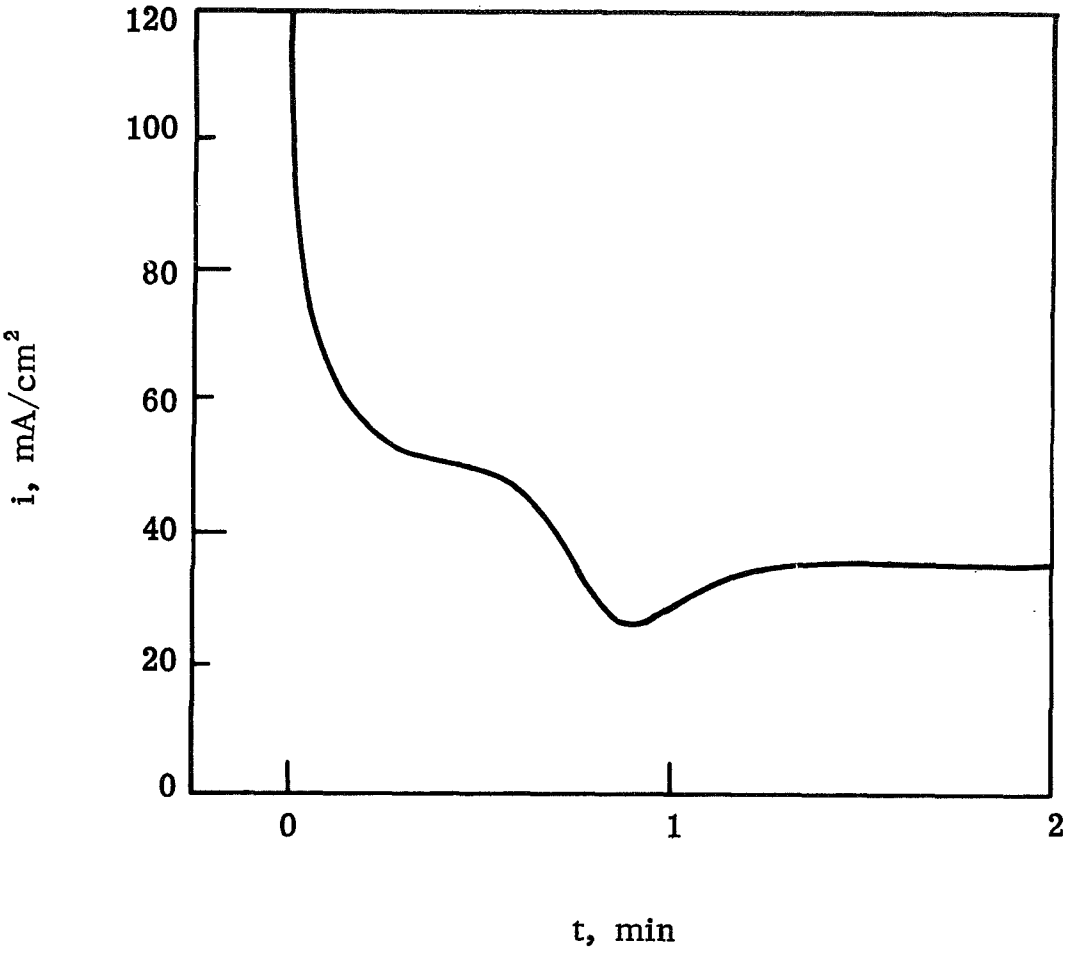

Fig. 35. Anodic current as a function of time upon potentiostatic polarization of Al working electrode at 150 mV versus Al in $AlCl_3$-KCl-NaCl (57.5-12.5-30 mol %) at 126 °C (no i-R correction)

the initial $AlCl_3$ concentration until passivation appears. Parallel to the behavior of Fig. 30, one observes that the Al electrode, which is shiny after cathodic polarization, assumes a very dull appearance upon passivation. The fact that in Fig. 30 the anodic and cathodic charges are almost equal indicates a rather compact diffusion layer with practically no convection. As the cathodic prepolarization time is increased above the values shown in Fig. 30, the charge obtained prior to anodic passivation becomes smaller than the cathodic charge, as one would expect.

Cathodic behavior. -- If the above explanation holds, we should expect a similar passivation effect at cathodic currents. In fact, current-voltage sweeps show indications of such a behavior (Figs. 28 and 32 through 34). In all cases, however, a subsequent current increase is found after indications of passivation. This is due to dendrite formation at the Al electrode. Long, shiny, Al dendrites can easily be seen growing into the electrolyte, thus enlarging the active surface area.

Again, dendrite growth is not directly connected to potential but rather to current and time. There seems to be a current value below which little dendrite formation is noticeable. This limit changes with conditions. In some experiments, such as those in Fig. 30, it was observed that cathodic currents at a set potential stayed constant for a certain time and then began to increase as a consequence of dendrite formation. Although more detailed information on the parameters governing dendrite formation is required, our results indicate the strong effect of concentration polarization and/or ionic conductivity on dendrite formation.

Effect of Melt Composition

Information on the effect of melt composition can be obtained by comparing Figs. 27, 31, and 34 (obtained at 157 °C) or 28 and 32 (obtained at 105 °C). The most obvious difference between the melts is the much higher, steady-state, anodic current after passivation in melts II and III (Figs. 31 and 34). On the cathodic side, a deviation from the linear current-potential behavior appears at much larger current densities in melt I than in melt II (compare Figs. 28 and 32). This again confirms our explanation of salt formation at the electrode. Melt II, which is less concentrated in $AlCl_3$, can support higher anodic current densities (that means it can accept more Al^{3+} without forming insoluble $AlCl_3$) than melt I. The latter, however, since it is more concentrated in $AlCl_3$, will be able to support higher cathodic currents before forming a passivating salt layer due to $X\text{-}AlCl_4$ precipitation (we disregard for the moment the additional complication of dendrite formation). The anodic current maxima in Figs. 31 and 33 are very likely due to supersaturation of the melt close to the electrode. After the first crystals have formed, the supersaturation breaks down. This is responsible for the following current dip.

The same effect can be seen in Fig. 35, which shows the anodic current as a function of time upon potentiostatic polarization. Thus, the limiting value of the steady-state current, besides depending on the usual transport properties, also depends on the capacity of the melt

to accommodate concentration changes without surpassing the solidus line of the phase diagram. The latter is clearly a function of melt composition.

Effect of Temperature

The effect of temperature on the current-voltage behavior of the Al electrode in the molten salt electrolyte can be seen most clearly by comparing Figs. 31 and 32 or 33 and 34, obtained using the same melt. Although a considerable steady-state current can be obtained at 157 °C (~50 mA/cm^2 in melt II and ~100 mA/cm^2 in melt III), this steady-state current is practically zero at 105 °C.

The temperature affects the results in several ways. First, there is the temperature dependence of the usual transport phenomena; for example, the viscosity decreases, and the diffusion coefficients increase with rising temperature. Much more important in our case, however, are considerations concerning the $AlCl_3$-KCl-NaCl phase diagram. We mentioned earlier the key role of solid salt formation. How large a concentration change is necessary to surpass the solidus line of the phase diagram is, to a large extent, a function of temperature (besides initial melt composition). That transport phenomena are current-limiting has been established qualitatively by stirring and quantitatively by the use of a rotating Al disk. The results of these experiments are described below.

The temperature will surely have an effect on dendrite growth, since this is controlled by diffusion and ohmic polarization. Further changes in conductivity due to varying dissociation constants and changes in complex formation with temperature are to be expected. These problems can, however, not be discussed more closely on the basis of presently available data.

Effect of Mass Transport

All results of our stationary polarization measurements at Al electrodes indicate that the anodic limiting currents are a function of the mass transport in the melt. We therefore expect the anodic limiting currents to depend on the diffusion layer thickness and thus on the rotation rate of a rotating Al disk electrode.

The rotating disk arrangement was described earlier in connection with the mechanism of chlorine reduction. The electrode was made by press-fitting a cylindrical piece of pure Al into Teflon. The results of these experiments in $AlCl_3$-KCl-NaCl (57.5-12.5-30 mol %) at 125 °C are summarized in Fig. 36. This figure shows the variation of the anodic limiting current, at different Al electrodes and at different potentials, on the limiting current plateau as a function of the square root of the angular velocity.

As mentioned earlier, the limiting current at a rotating disk electrode for a reaction which is controlled only by mass transfer is given by Levich (Ref. 28):

$$i_L = (\text{constant})\, nFD^{2/3}\, \upsilon^{-1/6}\, \omega^{1/2}\, \Delta C$$

where the value of the constant is approximately 0.620, D is the diffusion coefficient, ΔC is the

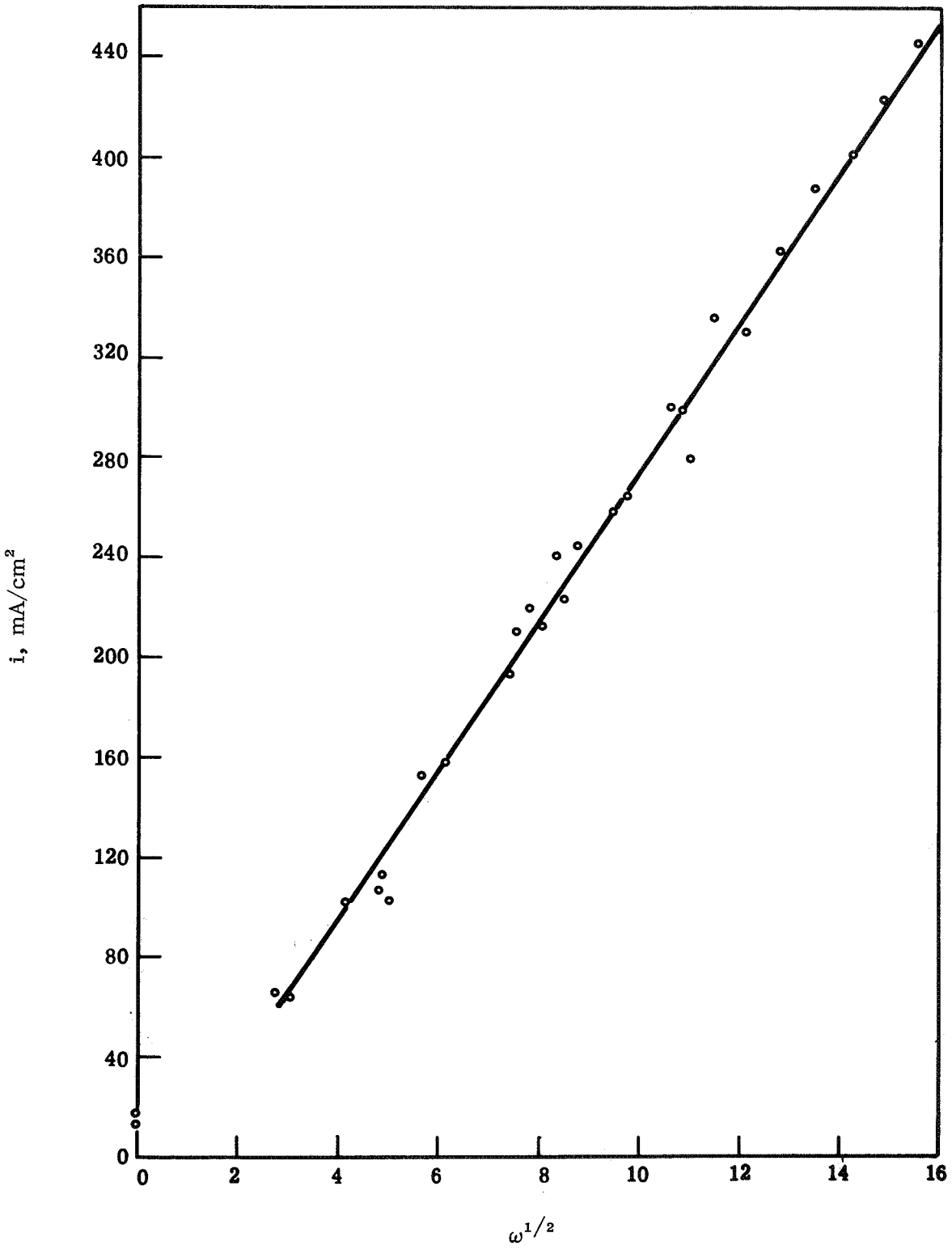

Fig. 36. Anodic limiting current at rotating Al disk electrode in $AlCl_3$-KCl-NaCl (57.5-12.5-30 mol %) at 125 °C

concentration gradient of the electroactive species, υ is the viscosity, and $\omega = 2\pi(\text{rps})$, where rps = rotations per second. This equation implies a linear relationship between i_L and $\omega^{1/2}$ under diffusion controlled conditions.

As Fig. 36 shows, the experimental data can indeed be represented very well by a straight line in such a plot. The slight deviations from linearity and some variations in the individual current densities were to be expected. One must keep in mind that here we are actually dealing with the dissolution of a passivating solid salt layer at the rotating electrode, which is in many respects quite different from the idealized conditions for which the above equation is strictly valid. Further, at the high current densities observed, changes in the electrode itself cannot be avoided.

These results show clearly, however, the role of transport phenomena in removing reaction products from the electrode surface. They show further that high current densities can be obtained at Al electrodes at relatively low temperature if the transport limitations can be overcome.

Microscopic, In Situ Observation of the Al Electrode During Polarization

Experimental. -- The experimental cell consisted of a 100-ml, round-bottom, four-neck Pyrex flask with a flat Pyrex glass window at the bottom (see Fig. 37). The disk electrode was press-fitted into Teflon tubing and extended about 6 mm from the glass window. The counter-electrode consisted of several loops of Al wire. A rubber balloon was used as a flexible argon reservoir. All connections were made with standard taper Teflon connectors containing O-ring press fittings. For measurements, the cell was heated in the hot air bath of a small oven containing a hole (1.5-cm diameter) in the bottom for microscopic observation. The basic set-up, with the Leitz metallograph, is shown in Fig. 38 (exploded view).

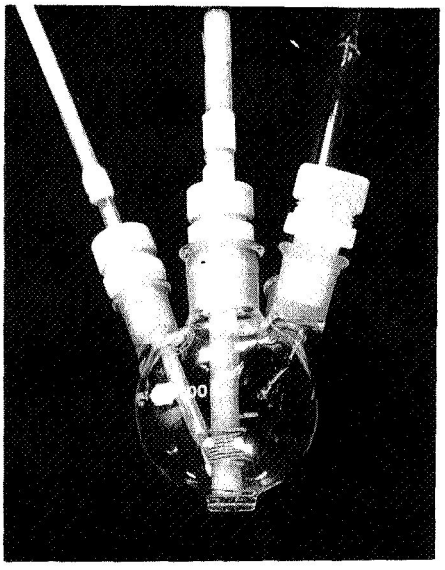

Fig. 37. Cell for in situ microscopic observation of a disk electrode

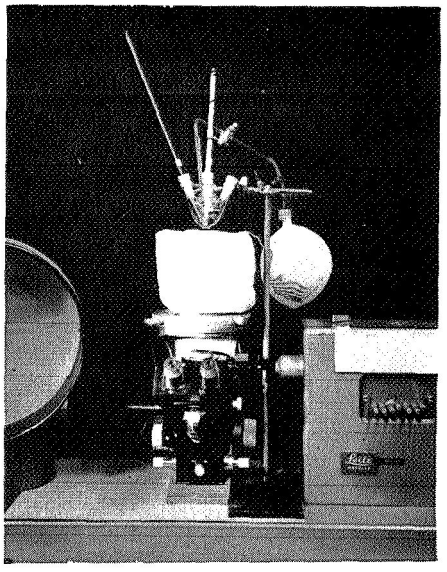

Fig. 38. Experimental setup for in situ microscopic observation (exploded view)

Results.-- The experiments were conducted in the $AlCl_3$-KCl-NaCl melt (57.5-12.5-30 mol %) at 133 °C. Figs. 39 through 42 show the electrode at different stages of polarization.

Fig. 39. Dendrites at Al electrode (25X) in $AlCl_3$-KCl-NaCl (57.5-12.5-30 mol %) at 133 °C

Fig. 40. Al electrode covered by passivating salt layer (25X) in $AlCl_3$-KCl-NaCl (57.5-12.5-30 mol %) at 133 °C

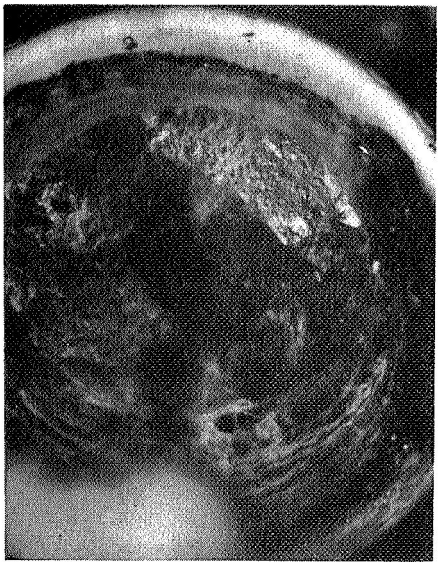

Fig. 41. View through a gas bubble on anodically polarized Al electrode (25X) in $AlCl_3$-KCl-NaCl (57.5-12.5-30 mol %) at 133 °C

Fig. 42. Area of anodically polarized Al electrode after gas bubble left (25X) in $AlCl_3$-KCl-NaCl (57.5-12.5-30 mol %) at 133 °C

The electrode had an etched surface which appeared as dark and bright planes in partially polarized light. The formation of gas bubbles could also be observed. They appeared to form mainly on the Al surface, more or less independently of polarization. Only at an anodically passivated electrode was a markedly decreased rate of bubble formation observed. The nature of this gassing is not completely clear at present. The most likely explanation seems to be a supersaturation of the melt with argon, or a slow decomposition of organic material leading to the formation of small bubbles at the Al-melt interface, which will also grow by incorporation of $AlCl_3$ vapor.

Fig. 39 is an example of dendrites formed at the electrode during cathodic polarization. Below 50 mA/cm^2, there seemed to be little dendrite formation; at higher current densities (up to 263 mA/cm^2), heavy dendrite formation could be observed. Upon reversing the current, the dendrites partially dissolved anodically, and separated from the electrode.

A sufficiently high anodic current led to passivation of the electrode due to salt formation (see Fig. 40). Fig. 41 shows an area of the Al electrode through a larger gas bubble which shielded the surface from the anodic current. After the bubble left the electrode, a bright reflecting area appeared (Fig. 42), which then turned into the passivated state (Fig. 40).

It was quite interesting to watch the growth of a gas bubble at the passivated electrode. One could observe strong motion at the gas-electrode-melt interface accompanied by transport of solid salt along the gas-liquid interface to the top of the bubble. This salt seemed to disappear by partial evaporation into the bubble and by dissolution in the melt. Thus, the electrode area underneath the bubble was not covered by a passivating layer, but appeared equal to an etched electrode in the gas phase. Occasionally, one could see circular residues from an incompletely decomposed passivation layer (compare Fig. 41).

The behavior of the Al electrode, seen here by direct microscopic observation, agrees perfectly with our earlier findings, and further confirms our ideas of the processes occurring at the Al electrode in the molten salt electrolyte.

Relation Between Current and Activation Polarization

Preliminary measurements showed that the charge transfer processes at the Al electrode are quite fast. This means that the electrode processes are very reversible, and the observed overvoltages are mainly due to concentration polarization. It is therefore necessary to use transient methods to investigate the electrode kinetics. We chose galvanostatic pulse measurements for this purpose.

Galvanostatic current step methods. -- The galvanostatic technique, considering the double layer charging, was originally discussed by Berzins and Delahay (Ref. 37). Since then, it has been used in several investigations (Ref. 38). The change in potential resulting from the constant current through the electrode-melt interface is determined by the rate of charging of the double layer and the rate of mass transfer to the electrode, i.e.,

$$i = C_{dl}\frac{d\eta}{dt} + nFD\left(\frac{\partial C_o}{\partial x}\right)_{x=0} \qquad (12)$$

where the symbols have their usual meaning. For a metal activity of unity, and for the boundary conditions: $C_o = C_o^\circ$ when $x > 0$, and $t = 0$ and $C_o \rightarrow C_o^\circ$ when $x = \infty$ and $t > 0$:

$$nFD\left(\frac{\partial C_o}{\partial x}\right)_{x=0} = i_o\left\{\frac{C_o}{C_o^\circ}\exp\left(\frac{-\alpha n\eta F}{RT}\right) - \exp\left[\frac{(1-\alpha)n\eta F}{RT}\right]\right\} \qquad (13)$$

which gives

$$\eta = \frac{-i}{C_{dl}}\frac{1}{(A-B)}\left\{\frac{B}{A^2}\left[\exp(A^2t)\ \text{erfc}\,(At^{1/2}) + \frac{2\,At^{1/2}}{\pi^{1/2}}\right]\right.$$

$$\left.\times\frac{-A}{B^2}\left[\exp(B^2t)\ \text{erfc}\,(Bt^{1/2}) + \frac{2\,Bt^{1/2}}{\pi^{1/2}} - 1\right]\right\} \qquad (14)$$

for $\eta < (0.1\ RT/nF)$ $(\sim 5\ mV)$,

where

$$A = \frac{i_o}{2\,nFC_o^\circ D^{1/2}} + \left[\frac{i_o^2}{4\,n^2F^2(C_o^\circ)^2D} - \frac{nFi_o}{RTC_{dl}}\right]^{1/2}$$

and

$$B = \frac{i_o}{2\,nFC_o^\circ D^{1/2}} - \left[\frac{i_o 2}{4\,n^2\,F^2(C_o^\circ)^2D} - \frac{nFi_o}{RTC_{dl}}\right]^{1/2}$$

For $t > 50/B^2$, Eq. (14) approximates, within 1%, to

$$\eta = \frac{-2\,RTit^{1/2}}{\pi^{1/2}n^2F^2C_o^\circ D^{1/2}} + \frac{RTi}{nF}\left[\frac{RTC_{dl}}{n^3F^3(C_o^\circ)^2D} - \frac{1}{i_o}\right] \qquad (15)$$

Hence, a plot of $\eta/t^{1/2}$ should give a straight line of slope

$$\frac{d\eta}{d(t^{1/2})} = \frac{-2\,RTi}{\pi^{1/2}n^2F^2C_o^\circ D^{1/2}} \qquad (16)$$

from which a value for $C_o^\circ D^{1/2}$ can be calculated.

When $t^{1/2} = 0$, then

$$\eta = \frac{RTi}{nF}\left[\frac{RTC_{dl}}{n^3F^3(C_o^\circ)^2D} - \frac{1}{i_o}\right] \qquad (17)$$

and the intercept on the η axis, together with the value for $D(C_o^\circ)^2$ calculated above, will give a value for i_o from Eq. (17).

An alternative method for calculating i_0 is the use of a special value of $t^{1/2}$ given by

$$t_c^{1/2} = -\frac{\pi C_{dl}}{4\,i} \times \frac{d\eta}{d(t^{1/2})} \qquad (18)$$

The corresponding overpotential, η_c, can be found from the curve, and a value for i_0 calculated from the equation

$$\eta_c = -\frac{RT}{nF} \times \frac{i}{i_0} \qquad (19)$$

Both of these methods depend on the determination of the differential double layer capacity which can be ascertained by the initial slope of the potential-time trace at sufficiently short times. One can show (Ref. 39) that for the error of C_{dl} to be less than m%, the maximum time, t_m, to which the measurement of the slope can be extended is $t_m = 2\,mRTC_{dl}/100\,nFi_0$. Thus, for example, if a double layer capacitance of 40 μF is to be measured to better than 50%, and i_0 = 250 mA/cm^2, then the slope of the potential-time trace has to be measured at times shorter than 2 μsec.

Experimental. -- In view of the facts mentioned above, it was necessary to use pulses with a very short rise time and high current density. It was also necessary to be able to record small potential changes with time, which required a low noise level in the experimental setup and compensation of the ohmic drop in the solution. Fig. 43 is a schematic of the measuring circuit. For the constant current pulses, the output of a Wavetek function generator was used directly. This instrument was gated by a Tyco-built pulse generator to allow multiple pulse

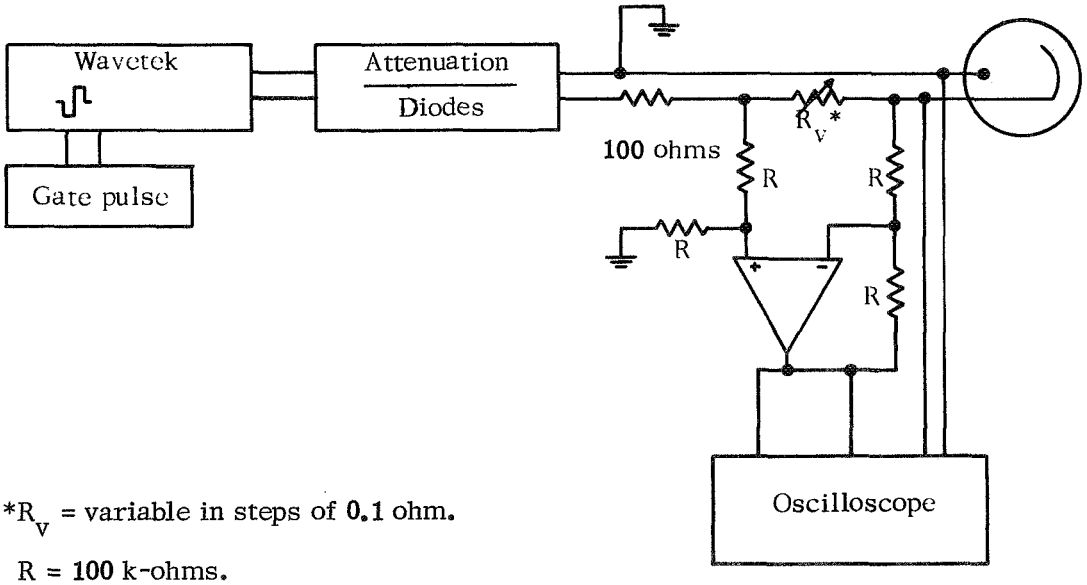

*R_v = variable in steps of 0.1 ohm.

R = 100 k-ohms.

Fig. 43. Schematic diagram of measuring circuit for galvanostatic pulse experiments

application. By the use of two diodes, either cathodic or anodic current pulses could be selected. A dual trace oscilloscope (Tektronic 556 with two type W plug-in units) was used to record current and potential as a function of time. Current was measured by the potential drop across a known resistance. The i-R compensated, potential-time traces were obtained by feeding the potential of the two-electrode cell and the output of the i-R compensator into the inputs of the differential amplifier. The measurements were conducted at an Al disk electrode (0.385 cm^2). A 15-cm^2 sheet of pure Al (Alpha Chemical Co.) served as the counterelectrode. The electrolyte was $AlCl_3$-KCl-NaCl (57.5-12.5-30 mol %). Since the freshly prepared melt showed some gassing, the temperature was raised and kept at 160 °C for about 2 hr. At that time, all gassing had stopped, and the temperature of the melt was lowered to 130 °C and kept constant at this value by a temperature controlled silicone oil bath, as described earlier. Again, a slightly positive argon pressure was kept in the cell at all times.

Results. -- Figs. 44 and 45 show two typical, oscilloscopic, potential-time traces at anodic and cathodic current pulses. From the initial slope of the galvanostatic potential-time curves, we determined an average value for the double layer capacity of 40 ± 10 $\mu F/cm^2$. Considering the surface roughness, one would expect to find a double layer capacity of approximately this size in the absence of specific adsorption effects.

Fig. 46 is an example of overvoltage versus square root of time plots, at various current densities, according to Eq. (15). At times larger than 10 μsec, the potential varies linearly with $t^{1/2}$. As expected, the slope of these lines increases with increasing current density. The times, $t_c^{1/2}$, according to Eq. (18) are also included in Fig. 46. The results of these measurements are summarized in Table IV. The first column lists the current density

TABLE IV

EXCHANGE CURRENTS AND MASS TRANSPORT FACTORS AT THE Al ELECTRODE AT 130 °C

i, mA/cm^2	η_c, mV	$C_\delta^* D^{1/2}$ $(mol/cm^2 sec^{1/2}) \times 10^{-8}$	i_0, mA/cm^2
			Anodic
58	2.5	1.39	266
58		1.61	267
88	3.8	1.06	264
88		1.59	266
121	6.0	0.81	229
121		0.59	225
167	8.5	1.10	225
			Cathodic
27.8	1.2	1.39	266
48.8	2.0	1.47	280
62.5	2.55	1.76	282
71.2	3.05	1.46	268
185.0	7.5	1.49	283
185.0	8.0	1.49	266

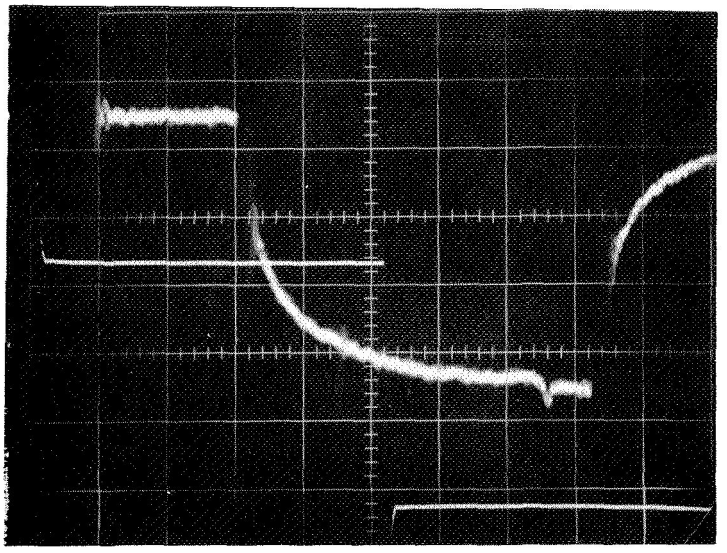

Fig. 44. Anodic, galvanostatic, potential-time curve at Al electrode in $AlCl_3$-KCl-NaCl (57.5-12.5-30 mol %) at 130 °C (i = 167 mA/cm^2, ordinate scale = 5 mV/div, abscissa scale = 10 μsec/div)

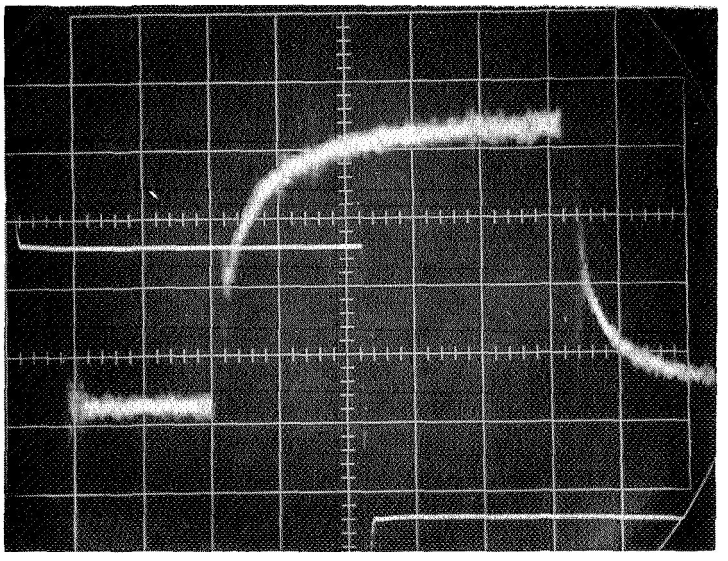

Fig. 45. Cathodic, galvanostatic, potential-time curve at Al electrode in $AlCl_3$-KCl-NaCl (57.5-12.5-30 mol %) at 130 °C (i = 185 mA/cm^2, ordinate scale = 5 mV/div, abscissa scale = 10 μsec/div)

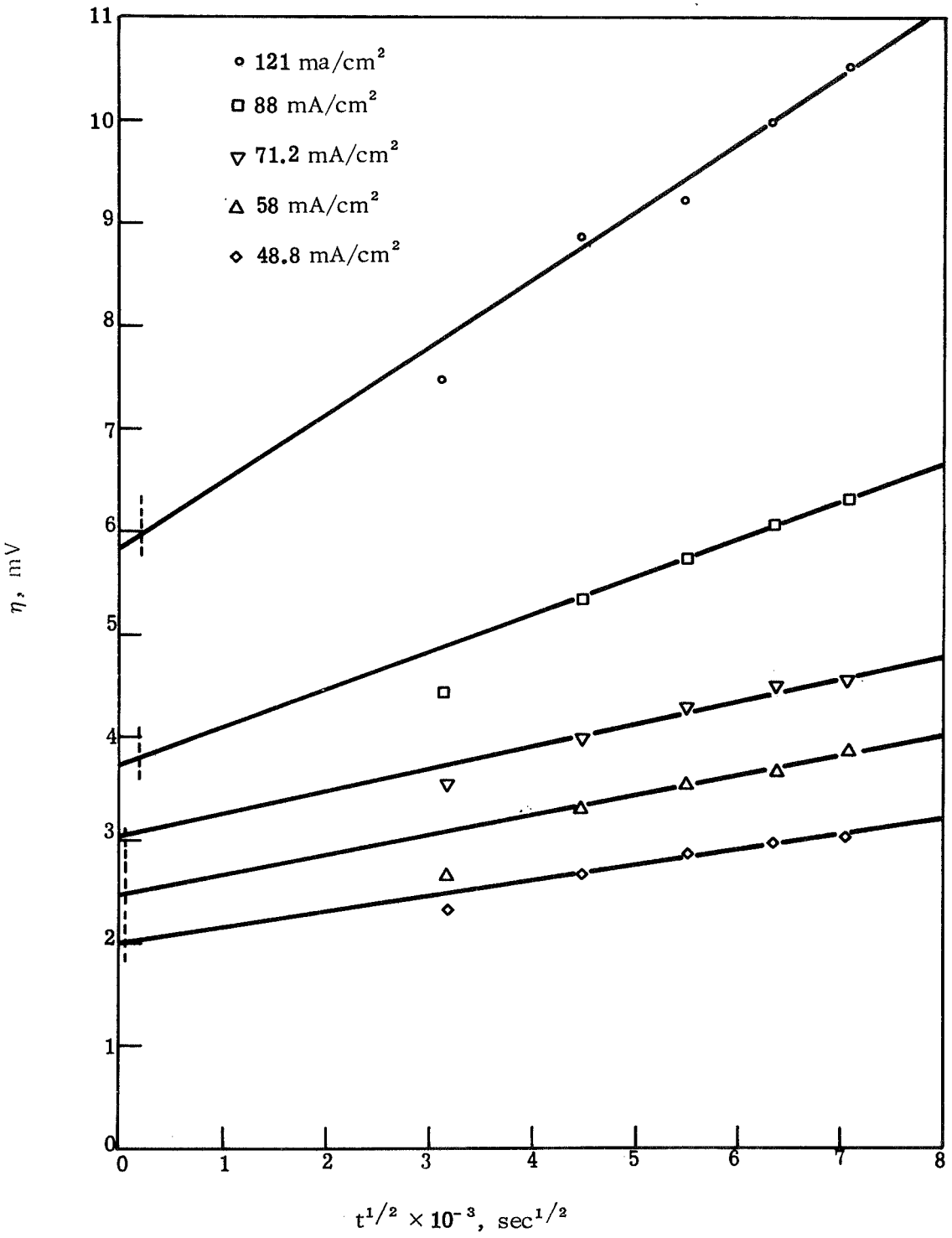

Fig. 46. Variation of overvoltage with time at Al electrode upon galvanostatic current step in $AlCl_3$-KCl-NaCl (57.5-12.5-30 mol %) at 130 °C

(per geometric cm^2). The second column gives the overvoltages, η_c, obtained from a plot of η versus $t^{1/2}$ at time $t_c^{1/2}$. The third column gives values for the parameter $C_0^0 D^{1/2}$ calculated from Eq. (16), using the slope of the straight lines from η versus $t^{1/2}$ plots. Finally, the last column gives values for the apparent exchange current calculated from Eq. (17). Fig. 47 shows a plot of i versus η.

At low overvoltage, one finds a linear relationship between current density and potential. From the slope at $\eta = 0$, one obtains again an exchange current according to Eq. (19). With n = 3, the apparent exchange current at the Al electrode was $i_0 = 268$ mA/cm^2 at 130 °C in the melt $AlCl_3$-KCl-NaCl (57.5-12.5-30 mol %). It is worth noting that there is no change in slope upon passing from anodic to cathodic overpotentials. This does not necessarily mean that we deal with the same rate-determining step in the anodic and cathodic electrode reaction. It shows, however, that the anodic and cathodic exchange currents are equal.

If we assume that the cathodic and anodic rate-determining steps are equal, the current potential relationship can be represented by:

$$i = i_0 \{\exp(-\alpha z F\eta/RT) - \exp[(1-\alpha) zF\eta/RT]\} \qquad (20)$$

We can then use a plot which is valid regardless of the overvoltage, as was introduced by Allen and Hickling (Ref. 40). The above equation can be rewritten

$$\frac{i}{1-\exp(zF\eta/RT)} = i_0 \exp(-\alpha zF\eta/RT)$$

Thus

$$\ln \frac{i}{1-\exp(zF\eta/RT)} = \ln i_0 - \frac{\alpha zF}{RT}\eta \qquad (21)$$

The slope of a plot of Eq. (21) yields α, and the intercept at $\eta = 0$ gives the exchange current.

Fig. 48 shows a plot of Eq. (21), with the current-potential data obtained from the galvanostatic pulse measurements discussed above. The number of electrons transferred in the rate determining step, z, is varied from one to three. The calculated points can be represented fairly well by straight lines from whose slope one obtains the following values of α:

z	α
1	1.0
2	0.7
3	0.64

Thus, the experimental results could be reasonably explained by a reversible two- or three-electron transfer step. Even though multiple electron transfer is less probable than the transfer of a single electron, it has been observed in molten salts (Ref. 41). The range of the presently available data is, however, not sufficient to decide upon a detailed mechanism of electron transfer at the Al electrode in the molten salt electrolyte.

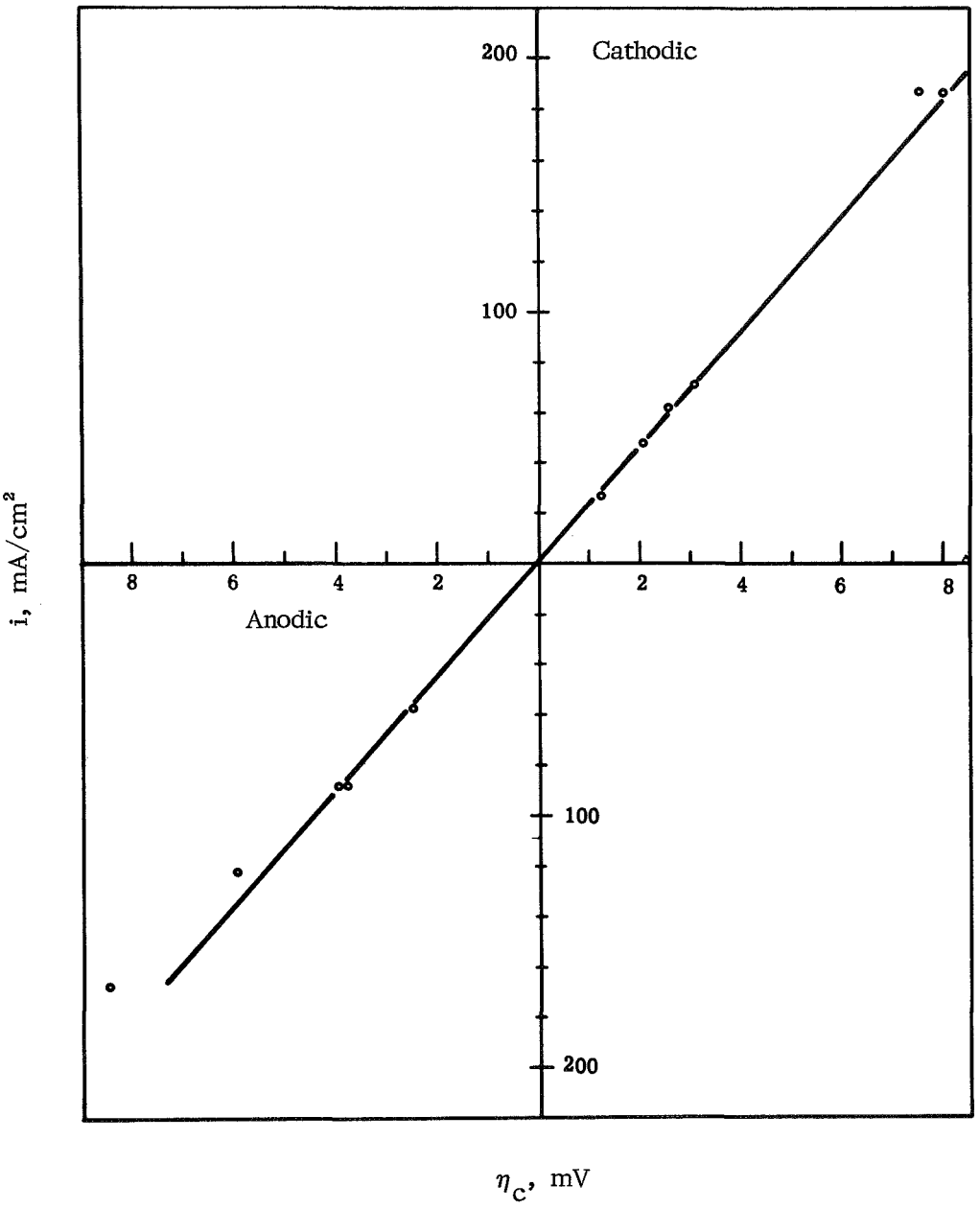

Fig. 47. Current density versus activation overvoltage at Al electrode in $AlCl_3$-KCl-NaCl (57.5-12.5-30 mol %) at 130 °C

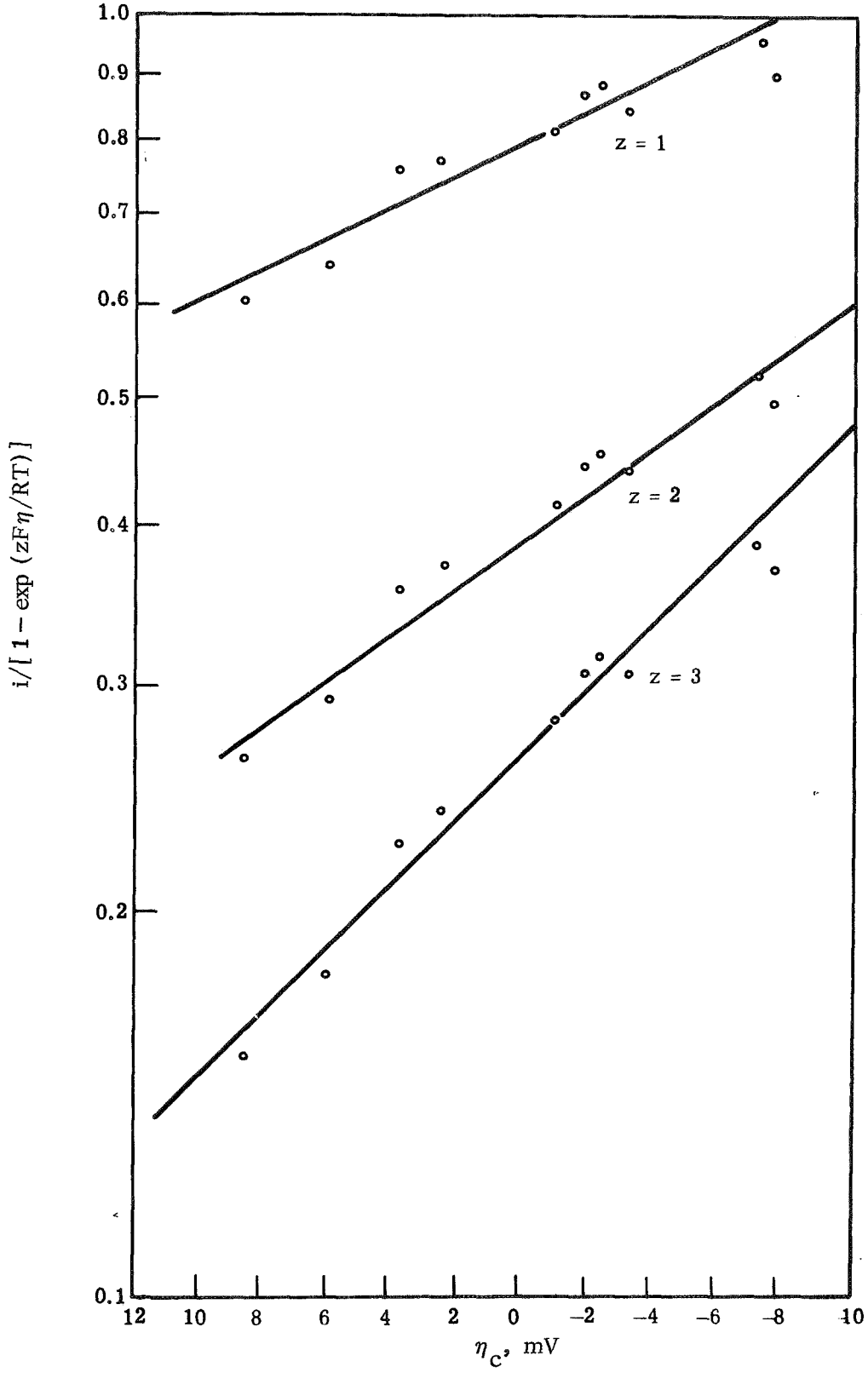

Fig. 48. Allen-Hickling plot of current-potential data at Al electrode in $AlCl_3$-KCl-NaCl (57.5-12.5-30 mol %) at 130 °C

Finally, it is quite interesting to examine more closely the values obtained for the transport parameter, $C_0^\circ D^{1/2}$. These values were found to be approximately 1.4×10^{-8}. Let us assume a diffusion coefficient of 10^{-6} cm^2/sec for the active species, similar to the value determined earlier for Fe^{3+}. Hence, we obtain $C_0^\circ \approx 1.4 \times 10^{-5}$ mol/cm^3. For comparison, we can calculate the total $AlCl_3$ concentration in the melt to be $\sim 9.4 \times 10^{-3}$ mol/cm^3 (using an estimated value of 1.7 g/cm^3 for the density). If we consider only the $AlCl_3$ not complexed as $KAlCl_4$ or $NaAlCl_4$, we would still have $\sim 1.2 \times 10^{-3}$ mol/cm^3 in our melt. Thus, the measured parameter, $C_0^\circ D^{1/2}$, suggests a relatively low concentration of the electroactive species, probably caused by further complex formation. Since practically nothing is known about the complex formation in $AlCl_3$-rich melts, this interesting subject cannot be discussed further.

Recently, Del Duca investigated the electrochemical behavior of the Al electrode in molten $AlCl_3$-NaCl and $AlCl_3$-(LiCl-KCl) eutectic electrolytes in the temperature range 175 to 313 °C (Ref. 42). The apparent exchange currents varied from 1 to 56 mA/cm^2, and surface diffusion was found to be the rate-determining step at low overpotentials. At high overpotentials, the most probable anodic rate-determining step was given as $Al \rightarrow Al^+ + e^-$, and the most probable cathodic rate-determining step in $AlCl_3$-NaCl electrolyte was given as $Al^{2+} + e^- \rightarrow Al^+$.

Conclusions. -- The behavior discussed above in detail leads us to the following conclusions:

1. The passivation effect is due to the formation of a solid salt layer at the electrode surface caused by concentration changes during current flow.

2. The occurrence of passivation is not dependent on potential, but rather on current and time, i.e., on charge passed through the electrode. It also depends on the transport properties of the melt.

3. The occurrence of salt formation depends on the compositional stability of the melt towards concentration changes. It is strongly dependent on melt composition (see phase diagram) and on temperature.

4. At cathodic currents, dendrite formation occurs at the Al electrode. Detailed conditions would have to be investigated.

5. The Al electrode itself is highly reversible and able to support large current densities at low activation overvoltage.

6. The polarization observed in the experiments is almost completely ohmic in nature. It again depends on melt composition and temperature.

FEASIBILITY TEST OF Al/Cl_2 CELL

In order to demonstrate the feasibility of an Al/Cl_2 battery with $AlCl_3$-KCl-NaCl electrolyte, a cell was built using a porous carbon electrode as the chlorine electrode, and operated in the primary mode. Fig. 49 shows the chlorine cathode arrangement. The porous electrode was made from a sample of Speer Pure Carbon no. 37 (previous work had shown this to be corrosion resistant). The material had been machined to give a cylinder 4.5 cm high and 1.9 cm in diameter, with an internal concentric hole 0.3 cm penetrating to 0.8 cm of the base of the cylinder. The cylinder was externally threaded at the open end and was screwed to an internally threaded Teflon tube. Electrical contact was made by means of a platinum wire attached to the thread.

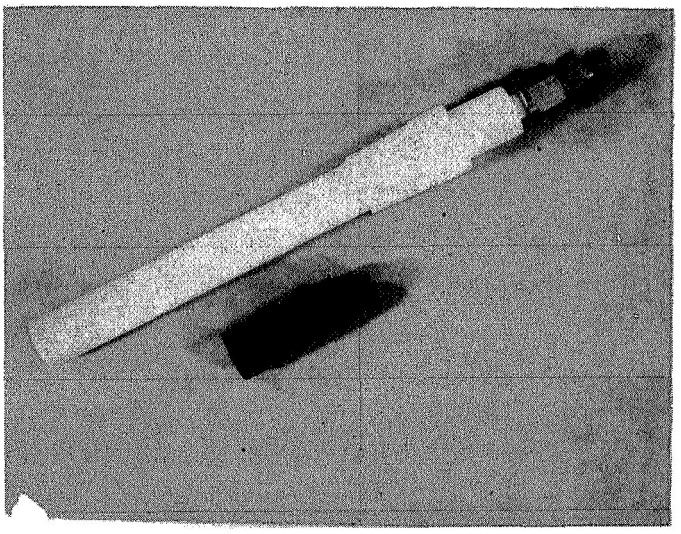

Fig. 49. Porous carbon electrode

Fig. 50 shows the cell arrangement. The Al electrode was a cylinder (73 cm^3) 5.3 cm high and 4.3 cm in diameter concentric to the carbon cylinder. An Al reference electrode was placed in a glass tube external to the Al cylinder, with a Luggin capillary which was introduced through a hole in the Al electrode so that the tip of the Luggin capillary was 2 mm from the carbon electrode. The electrolyte was a mixture of $AlCl_3$, KCl, and NaCl (66-14-20 mol %). The operating temperature was 150 °C. The chlorine electrode was operated at a pressure of about 10 psig, which allowed a slight bubbling of chlorine (this pressure had been adjusted to give the highest current density). The curve in Fig. 51, obtained with this cell, shows that an Al/Cl_2 cell can be built with at least 20 mA/cm^2 over 1.8 V cell potential, using a noncatalyzed carbon electrode. The cell was operated potentiostatically, but was briefly discharged through a resistor to confirm its capacity to generate power.

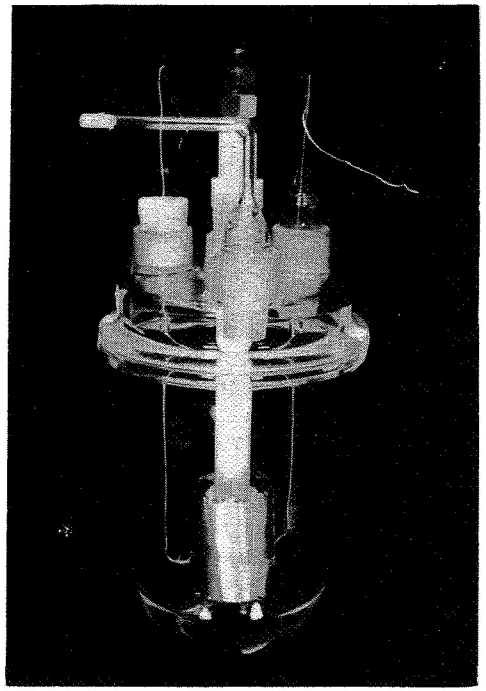

Fig. 50. Cell arrangement for feasibility test of Al/Cl_2 battery

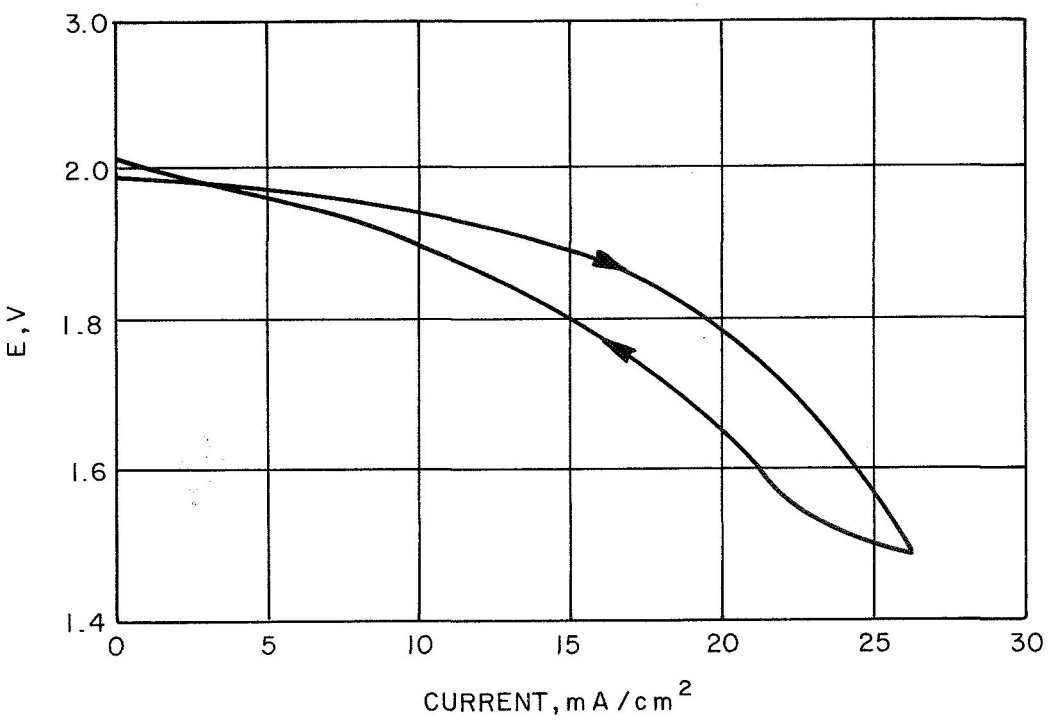

Fig. 51. Stationary current-voltage behavior of experimental Al/Cl_2 cell (porous Speer carbon no. 37 electrode; Cl_2 pressure = 10 psig; $AlCl_3$-KCl-NaCl = 66-14-20 mol %)

The performance to be expected from the Al electrode in an actual battery can be semi-quantitatively estimated from our measured exchange currents. Equally, the transient response can be estimated from concentration polarization measurements and from the determination of the effect of temperature and concentration on the steady-state current obtained with these electrodes.

The situation is more difficult with regard to the chlorine electrode because, since it is a gas diffusion electrode, its performance is highly dependent on the optimization of the electrode (especially in the discharge mode). However, we can use the parameters obtained with the rotating carbon disk electrode and compare them with similar parameters obtained for a well studied gas diffusion electrode (such as the oxygen electrode in KOH). In this way, we can extrapolate the performance for chlorine reduction which can be expected from a good electrode structure.

Table V shows the exchange currents and the transport coefficients (C × D factor) for the chlorine electrode and for the oxygen electrode. The values for the oxygen electrode refer to the Pt electrode at 80 °C in 30% KOH (Refs. 43 through 46). As Table V shows, the exchange current for the chlorine electrode on carbon is 200 times larger than for the oxygen electrode on Pt, while the transport coefficient is about 50 times larger. This is an encouraging finding, because the oxygen electrode under the specified conditions has been developed to support several hundred mA/cm^2 at tolerable polarization. It can be expected, therefore, that under transient conditions the chlorine cathode based on aporous carbon structure can be developed to sustain appreciable currents at low polarization. The situation will be somewhat different under steady state, because it can be expected that salt precipitation may occur due to formation of $AlCl_3$ during charge and $AlCl_4^-$ during discharge. The effect of electrode structure, operating temperature, and electrode concentration on the maximum steady-state currents that can be obtained before salt precipitation should be the subject of subsequent work.

TABLE V

EXCHANGE CURRENTS AND TRANSPORT PARAMETERS FOR THE CHLORINE ELECTRODE IN $AlCl_3$-KCl-NaCl AT 130 °C AND FOR THE OXYGEN ELECTRODE IN 30% KOH AT 80 °C

Electrode	i_o, A/cm^2	C × D (Electroactive Species), mol/cm sec
Chlorine	1×10^{-4}	$\sim 5 \times 10^{-11}$
Oxygen	5×10^{-7}	1×10^{-12}

REFERENCES

1. Grothe, H.: Z. Elektrochem., 53, 1949, pp. 362-9.

2. Fischer, W., and Simon, A.: Z. Anorg. Allg. Chem., 306, 1960, pp. 1-12.

3. Midorikawa, R.: J. Electrochem. Soc. Japan, 23, 1955, pp. 127-9.

4. Grothe, H., and Piel, C. A.: Z. Elektrochem., 54, 1950, pp. 210-5.

5. Delimarskii, Yu. K., Berenblyum, L. S., and Sheiko, I. N.: Zh. Fiz. Khim., 25, 1951, pp. 398-403.

6. Midorikawa, R.: J. Electrochem. Soc. Japan, 24, 1956, pp. 23-7.

7. Midorikawa, R.: J. Electrochem. Soc. Japan, 23, 1955, pp. 72-6.

8. Grothe, H.: Z. Elektrochem., 54, 1950, pp. 216-9.

9. Midorikawa, R.: J. Electrochem. Soc. Japan, 23, 1955, pp. 352-5.

10. Moss, R. H.: U. Microfilms, Ann Arbor, Mich., 64 pp., publ. no. 12, 730, Dissertation Abs., 15, 1955, p. 1325.

11. Morozov, I. S., and Simonich, A. T.: Zh. Neorg. Khim., II, 8, (Engl. pp. 311-21), 1957, pp. 1906-14.

12. Kryagova, A. I.: J. Gen. Chem. USSR, 9.

13. Yamaguti, Y., and Sisido, S.: J. Chem. Soc. Japan, 62, 1941, pp. 304-7.

14. Morozov, I. S., Korshunov, B. G., and Simonich, A. T.: Zh. Neorg. Khim., 1, 1956, pp. 1646-57. J. Inorg. Chem. USSR, 1, 1956, pp. 203-14.

15. Plotnikov, V. A., and Kalita, P. T.: J. Russ. Phys. Chem. Soc., 62, 1930, pp. 2195-202.

16. Chao, T.: U. Microfilms, Ann Arbor, Mich., 294 pp., publ. no. 3704, Dissertation Abs., 12, 1952, p. 459.

17. Morozov, I. S., and Tsegledi, L.: Zh. Neorg. Khim., 6, 1961, pp. 2766-75. J. Inorg. Chem. USSR, 6, 1961, pp. 1397-1042.

18. Midorikawa, R.: J. Electrochem. Soc. Japan, 24, 1956, p. 83.

19. Glenser, O., and Kleine-Weischede, K.: Liebig Ann. Chem., 659, 1962, p. 17.

20. Verdieck, R. G., and Yntema, L. F.: J. Phys. Chem., 46, 1942, p. 344.

21. Munday, T. C. F., and Corbett, J. D.: Inorganic Chemistry, 5, 1966, p. 1263.

22. Verdieck, R. G., and Yntema, L. F.: J. Phys. Chem., 46, 1942 p. 344.

23. Plotnikov, V. A., Kirichenko, E. J., and Fortunatov, N. S.: Zap. Inst. Khim. Akad. Nauk Ukr. R.S.R., 7, 1945, p. 159.

24. J. Giner and G. Holleck, report prepared under Contract No. NAS 12-688 for National Aeronautics and Space Administration (March 70). For sale by the Clearinghouse for Federal Scientific and Technical Information, Springfield, Virginia 22151. CFSTI price = $3.00.

25. Letisse, G., and Tremillon, B.: J. Electroanal. Chem., 17, 1968, p. 387.

26. Swinkels, D. A. J.: J. Electrochem. Soc., 113, 1966, p. 6.

27. Will, F.: J. Electrochem. Soc., 110, 1963, p. 145.

28. Levich, V. G.: Physicochemical Hydrodynamics. Prentice Hall, Inc., 1962. For a review of the rotating disk system, see Riddiford, A. C.: Advances in Electrochemistry and Electrochemical Engineering, Vol. 4--The Rotating Disk System, P. Delahay, ed., Interscience, 1966.

29. Vetter, K. J.: Z. Naturforsch., 7a, 1952, p. 328 and 8a, 1953, p. 823.

30. Frumkin, A. N., and Aikazyan, E. A.: Dokl. Akad. Nauk SSSR, 100, 1955, p. 315; Frumkin, A. N., and Aikazyan, E. A.: Izv. Akad. Nauk SSSR Otd. Khim. Nauk, 1959, p. 202.

31. Fraser, G. H., and Barradas, R. G.: J. Electrochem Soc., 112, 1965, p. 462.

32. Parsons, R.: Trans. Faraday Soc., 47, 1957, p. 1332.

33. Skundin, A. M., Palanker, V. Sh., and Bagotskii, V. S.: Elektrokhimiya, 2, 1966, p. 1453.

34. Frumkin, A. N., and Tedoradse, G. A.: Dokl. Akad. Nauk SSSR, 118, 1958, p. 530.

35. Frumkin, A. N., and Tedoradse, G. A.: Z. Elektrochem., 62, 1958, p. 251.

36. Triaca, W. E., Solomons, C., and Bockris, J. O'M: Electrochim. Acta, 13,1963, p. 1949.

37. Bergins, T., and Delahay, P.: J. Amer. Chem. Soc., 77, 1955, p. 6448; —, Z. Elektrochem., 59, 1955, p. 792.

38. Graves, A. D., Hills, G. J., and Inman, D.: Advances in Electrochemistry and Electrochemical Engineering, Vol 4--Electrode Processes in Molten Salts, P. Delahay, ed., Interscience, 1966.

39. Inman, D., Bockris, J. O'M, and Blourgran, E.: J. Electroanal. Chem., 2, 1961, p. 506.

40. Allen, P. L., and Hickling, A.: Trans. Faraday Soc., 53, 1957, p. 1626.

41. Senderoff, S., and Mellors, G. W.: J. Electrochem. Soc., 113, 66 (1966).

42. Del Duca, B. S.: NASA TN D-5503, NASA, Washington, D. C., October 1969.

43. Giner, J., and Hunter, C.: J. Electrochem. Soc., 116, 1969, p. 1124.

44. Walker, Jr., R. D.: 4th Semiannual Report on NASA Research Grant NGR 10-005-022, August 31, 1967.

45. Giner, J., Parry, J. M., and Swette, L.: Proceedings of the 5th Biennial Symposium on Fuel Cells, ACS; Advances in Chemistry, Series No. 90, Washington, D. C., 1968.

46. Report Q-8 (June 1967) by Tyco Laboratories to National Aeronautics and Space Administration Headquarters, on Contract No. NASW-1233.